Shear Properties of Earth's Inner Core

Hrvoje Tkalčić, Sheng Wang, Thanh-Son Phạm

Research School of Earth Sciences, The Australian National University, 142 Mills Road, Canberra, 2601, ACT, Australia

Abstract

Understanding how the Earth's inner core develops and evolves, including fine details of its structure and energy exchange across the boundary with the liquid outer core, helps constrain its age, relationship with the planetary differentiation, and other significant global events throughout Earth's history, as well as the changing magnetic field. Since its discovery in 1936 and solidity hypothesis in 1940, the Earth's inner core has never ceased to inspire geoscientists. However, while there are many seismological observations of compressional waves and normal modes sensitive to the inner core's compressional and shear structure, the shear waves that provide direct evidence for the inner core's solidity have remained elusive and reported only in a few publications. Further advances in the emerging correlation-wavefield paradigm, which explores waveform similarities, may hold the keys to refined measurements of all inner-core shear properties, informing dynamical models and strengthening interpretations of its anisotropic structure and viscosity.

- What are the shear properties of the inner core, such as the shear-wave speed, shear modulus, shear attenuation, and shear-wave anisotropy? Can they be measured seismologically and confirmed experimentally? This review is looking at the answers to these fundamental questions.

1. INTRODUCTION

The Earth's inner core (IC) is a ball smaller than ~1% of the Earth's volume, discovered 85 years ago (Lehmann 1936). Several years after its discovery, Birch (1940) proposed that the IC presented a phase transformation of iron from liquid to solid. The overlaying physical process taking place at the inner-core boundary (ICB) is a slow growth – solidification of the IC from a liquid iron-nickel alloy of the outer core (OC). The IC is coupled with the OC's shell through the transfer of material and heat, and this coupling actively affects the generation and variations of the geomagnetic field (e.g., Braginsky 1963; Buffett et al. 1996; Hollerbach & Jones 1993; Roberts 2008), dynamics of the lowermost mantle (e.g., Aubert et al. 2008; Gubbins et al. 2011), and even processes at the Earth's free surface (e.g., Biggin et al. 2015). Indeed, investigating and understanding the IC has fascinated geoscientists for its essential role in the evolution and dynamics of our planet (for a review of historical facts, see Tkalčić (2017)). For recent reviews on IC-related research topics from a perspective of different disciplines, see Deguen (2012), Hirose et al. (2013), Deuss (2014), Souriau & Calvet (2015), and Tkalčić (2015).

The solidification process and the consequent solidity of the IC can be characterized by its shear properties, the elastic and anelastic behaviors of a solid material to shear (transverse) deformation. Seismic observations are the primary probes to investigate the shear properties of the IC via the observations of Earth's free oscillations or normal modes (Alterman et al. 1959; Benioff et al. 1961) and seismic shear waves (Bullen, 1950; 1951). This is formally similar to seismological studies of other regions of the Earth. However, given that the IC is buried beneath multiple Earth shells, investigating its shear properties with seismology has been proven very challenging. Observations are elusive or even unlikely (Shearer et al. 2011) for seismic waves sensitive to the IC's shear properties. Furthermore, in the view of constituting IC materials and their shear properties, it is uncertain which type of iron crystal, hexagonal-close-packed (hcp) phase (e.g., Jeanloz and Wenk 1988; Steinle-Neumann et al. 2001; Stixrude & Cohen 1995), body-centered-cubic (bcc) phase (e.g., Belonoshko et

al. 2008; Calvet & Margerin 2008; Vočadlo et al. 2003) or their mixture (e.g., Mattesini et al. 2014), is stabilized in the IC. This uncertainty contributes to the difficulties in investigating the shear properties of the IC.

Despite these difficulties, recent studies have led to a clearer picture and kept researchers motivated in finding new techniques and methods for advancements. Most recently, harnessing shear-wave energy contained in the coda-correlation wavefield, Tkalčić & Phạm (2018) devised a method and made new observations that provided new opportunities and research directions. Here, we review historical and contemporary studies for the shear properties of the IC. First, we focus on detections of a solid IC and constraining shear-wave speed (Section 2). This is followed by presenting specific and detailed shear properties of the IC, including attenuation in shear (Section 3) and shear-wave anisotropy (Section 4). Finally, we discuss the existing challenges and new research directions (Section 5), especially method developments available in modern global seismology using seismic and correlation wavefields. We conclude with a discussion on future studies of shear attenuation and show two candidates for direct observations of PKJKP waves utilizing array seismology.

2. SOLIDITY AND SHEAR-WAVE SPEED OF THE INNER CORE

2.1. A Brief History of the Inner Core Discovery and Solidity Hypothesis

At the time Lehmann analyzed the Buller, June 16, 1929, and the Hawke Bay, February 2, 1931, earthquakes, the existence of the liquid core, and the core-mantle boundary (CMB) were well established (Lehmann, 1936). The two travel-time branches of compressional (P) waves traversing the core along the ray paths beyond about 155˚ of epicentral distance were well documented and labeled P'_1 and P'_2 (today referred to as PKIKP and PKPab, respectively). However, there was no adequate explanation for the compressional (P) wave arrivals extending beyond about 100˚ epicentral distance, forming the travel-time curve Lehmann labeled P'_3. It became clear to her that P waves diffracted

around the core-mantle boundary (CMB) on their way through the Earth's interior from the New Zealand earthquakes to northern Europe were too weak to explain relatively prominent arrivals of P'_3 on vertical components. Therefore, another likely possibility was an Earth model with an "inner core" with a discontinuous increase in compressional wave speed in the Earth's center. In Lehmann's model, the inner core boundary (ICB) was embedded in the liquid core and placed at a radius of 0.2205 of the Earth's radius (1404.8 km). This model predicted the P'_3 branch of seismic arrivals that consisted of retrograde reflections from the ICB and prograde refractions through it, extending from about 119° and merging with the P'_1 curve at about 155°. This prediction did not contradict the observations even though the radius of the IC was larger than its present-day values.

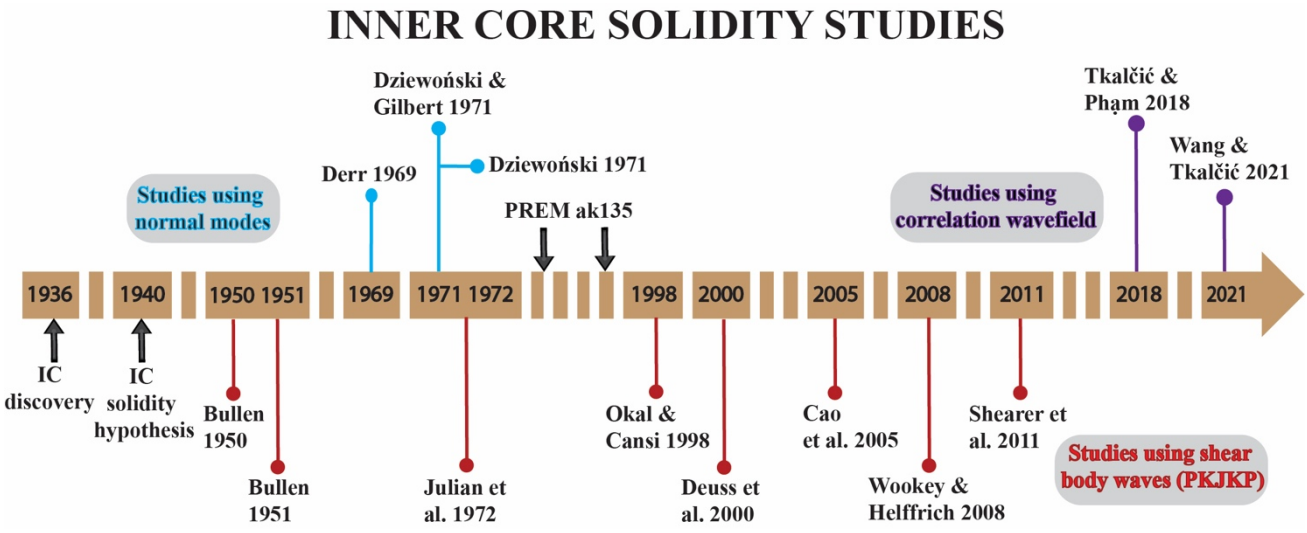

Figure 1

Timeline of the IC discovery (Lehmann 1936), its solidity hypothesis (Birch 1940), the two Earth models pertinent to the modern-day IC investigations: PREM (Dziewoński & Anderson 1981) and ak135 (Kennett et al. 1995), and significant publications investigating the IC solidity using three seismological approaches: normal modes, shear body waves, and coda-correlation wavefield.

It is worth pointing out that in Lehmann's hypothesis, the IC is merely a nucleus embedded in the liquid OC without explicit characterization of its aggregate state. Lehmann's assumed P-wave velocity values for the core and the IC were 8.0 km/s and 8.6 km/s. Indeed, such a velocity discontinuity was

sufficient in producing the observed travel-time curves without any assumptions on the IC's aggregate state. The IC was subsequently hypothesized to be solid in mineral physics studies of melting temperature of iron (Birch 1940; 1952). Assuming that temperature in the Earth's center reaches 4000˚ C and that temperature gradient is probably small in the core, Birch (1940) speculated that the outer part of the core might be molten, while an inner part could have remained frozen. This situation could account for Lehmann's seismologically observed velocity distribution in the core. In summary, while Lehmann discovered the IC (Lehmann, 1936), Birch hypothesized that it was solid (Birch, 1940) (Figure 1).

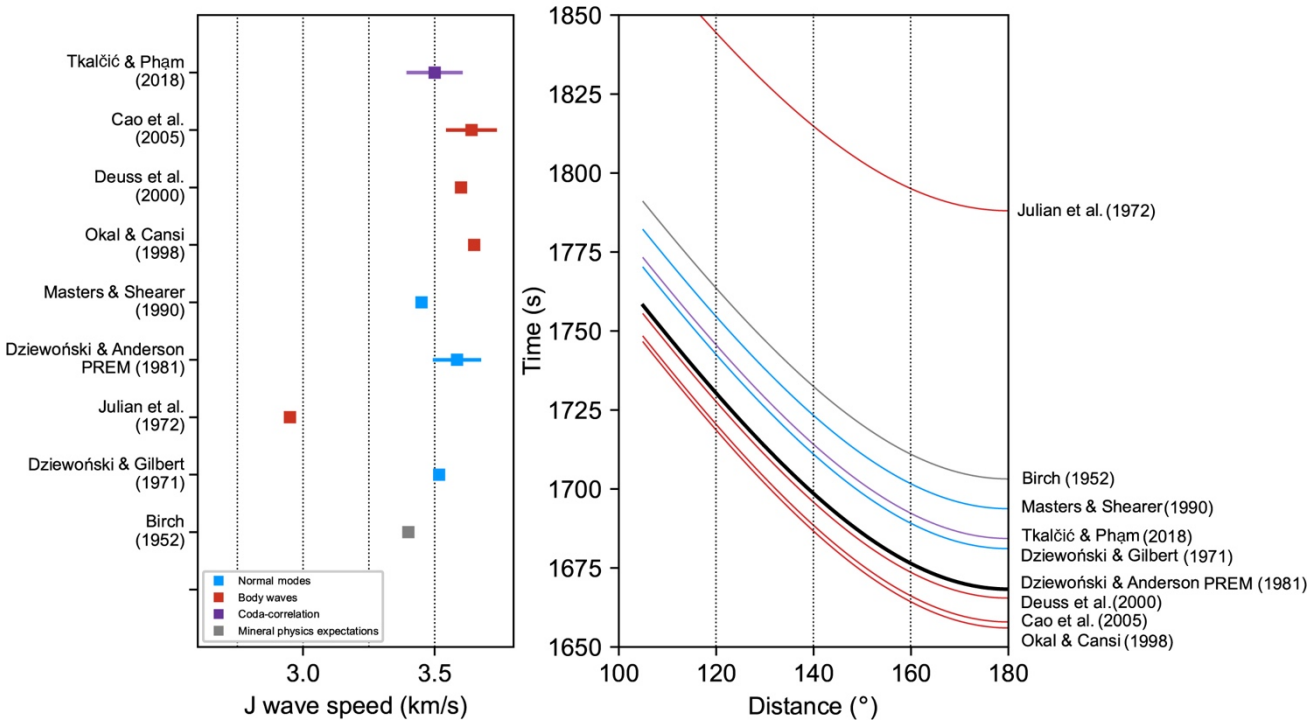

Figure 2

(left) Different values for J-wave speed, obtained in the IC-solidity studies. The colors depending on the seismological methods match those used in Figure 1, with a mineral physics estimate shown in grey. (right) According to the values given on the left, theoretical PKJKP travel-time curves are calculated for a source on Earth's surface. The PKJKP travel-time curve (thick black) for PREM is added for comparison.

The compressional-wave speed, V_P , can be defined as:

$$V_P = \sqrt{\frac{\kappa + 4\mu/3}{\rho}}, \quad (1)$$

where κ is the bulk modulus (incompressibility), ρ is the density, and μ is the shear modulus. If the IC is solid and embedded within the liquid OC, then μ will change from zero in the OC to a non-zero value in the IC. Such change can explain the increased V_P in the IC if assuming that the bulk modulus and density exhibit smooth variations with depth (Bullen 1946). With these assumptions, μ of the IC can be inferred from prior knowledge of ρ, κ and V_P according to Equation (1). The J wave speed, V_s can then be estimated as:

$$V_s = \sqrt{\frac{\mu}{\rho}}, \quad (2)$$

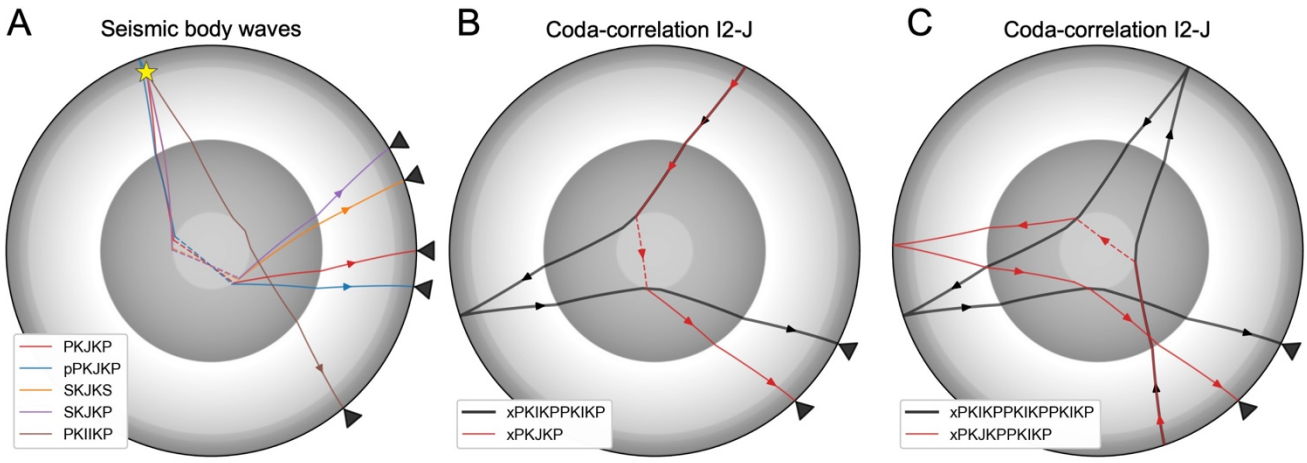

Figure 3

(A) Selected seismic body waves sensitive to shear properties of the solid IC. Dashed lines show shear waves in the IC (J waves). (B) Illustration of earthquake coda-correlation feature I2-PKJKP (hereafter called I2-J). The I2-J can be formed due to the similarity between two seismic waves: xPKIKPPKIKP (xI2) and xPKJKP (xJ), where "x" represents the common propagation legs for the two waves. Wave propagations corresponding to the "x" are not unique and are not shown, but they are discussed in the main text. (C) The I2-J, formed by another pair of waves: xPKIKPPKIKPPKIKP (xI3) and xPKJKPPKIKP (xJI). The J waves in (B) and (C) sample the IC in different directions, while they contribute to the same correlation feature, I2-J.

Using similar assumptions, Birch (1952) inferred that the IC is a crystalline iron with V_S=3.4 km/s. A grey symbol shows this estimate in Figure 2. Furthermore, Bullen (1950; 1951) calculated the theoretical travel times and amplitudes for the IC shear waves – a.k.a. PKJKP waves – as a function of epicentral distance. For the definition and a diagram of PKJKP waves through the Earth's interior, see Section 2.3. and Figure 3A. For the theoretical PKJKP travel-time curves for various estimates of IC shear-wave speed, see Figure 2. Therefore, at the beginning of the 1950s, it was established that seismological observations of IC shear waves would represent direct evidence of the IC's solidity, and the search for PKJKP could begin.

2.2. Normal Mode Studies

Indeed, the shear modulus and shear wave speed can be inferred from the observations of seismic body waves traversing different parts of the Earth, including the IC. However, the decades immediately following Birch's hypothesis did not yield reliable observations of those waves, despite numerous man-made explosions and expansion of seismic stations (Figure 1). What shifted the odds of the first observations from body waves to normal modes were the great earthquakes that occurred during the 1950s and the 1960s of the 20th century: the Kamchatka, M_w=9.0 earthquake of 1952, the Chile, M_w=9.5 earthquake of 1960, and the Alaska, M_w=9.2 earthquake of 1964. Those decades marked the time when the World Wide Standard Seismograph Network (WWSSN) analog data were digitized, and more sophisticated measurements of eigenfrequencies of normal modes became possible (Alterman et al. 1959; Benioff et al. 1961).

Normal modes of the Earth present a pattern of motion that samples the entire volume of the Earth, including the IC. They can take two forms: spheroidal ($_nS_l$), in which a particle undergoes both radial and tangential motion, and toroidal ($_nT_l$), where a particle undergoes a motion on a spherical surface. n is the radial order, and l is the angular order (e.g., Dahlen and Tromp, 1998). When n=0, the mode

165 is referred to as the fundamental mode, and if n>0, these modes are referred to as overtones. To observe
166 most IC-sensitive modes, the first 10 to 15 hours after the origin time of large earthquakes must be
167 discarded, and the time series must be converted to complex spectra in the frequency domain. A
168 frequency perturbation of a normal mode, δω due to a perturbation in bulk (κ) and shear modulus (μ)
169 of elasticity and density (ρ) is given by
170

$$\delta\omega = \int_0^a (\delta\kappa K_\kappa + \delta\mu K_\mu + \delta\rho K_\rho) dr, \quad (3)$$

171
172 where a is the normalized Earth's radius, and K_κ, K_μ, and K_ρ are the sensitivity kernels for κ, μ, and ρ
173 (defined in Section 2.1) as functions of radius r. Figures 2.15-2.17 in Tkalčić (2017) illustrate the
174 sensitivity of Earth's normal modes to IC structure. Although most normal modes have significant
175 energy in the Earth's mantle and the OC, several fundamental modes and overtones have substantial
176 sensitivity to shear-wave speed in the IC (e.g., ${}_{10}S_2$ and ${}_{13}S_2$).
177
178 Derr (1969) observed and identified a set of normal modes sensitive to the IC shear-wave speed:
179 fundamental modes ${}_0S_1$, ${}_0S_2$, and ${}_0S_3$, and their overtones ${}_1S_0$, ${}_1S_1$, ${}_1S_2$, ${}_2S_0$, ${}_2S_2$, ${}_2S_3$, and ${}_3S_0$. By analyzing
180 these observations and comparing them with the theoretical predictions (albeit without the corrections
181 for Earth's rotation and ellipticity), he concluded that the IC rigidity is plausible if the measurements
182 of some of the overtones were disregarded.
183
184 However, slightly later, Dziewoński (1971) and Dziewoński and Gilbert (1971) identified and utilized
185 more normal modes, noting that some of the modes listed in Derr (1969) were incorrectly identified.
186 Dziewoński (1971) combined normal mode data with the travel time data of PcP, ScS, and PKIKP
187 waves. He concluded that the IC must be rigid to satisfy the observed normal mode eigenfrequencies
188 and travel times simultaneously. Dziewoński and Gilbert (1971) found the theoretically predicted

behavior of eigenfrequencies by either increasing the IC rigidity or modeling IC as a liquid. An increase in rigidity caused the bulk modulus to increase, enhancing compressional energy while diminishing the shear energy of the IC sensitive modes. An introduction of the liquid IC, however, implied a physically implausible, denser OC. Therefore, when comparing predictions and observations, the existence of a solid IC was favored. The authors suggested that the non-zero shear modulus in the IC represented a logical and the simplest explanation for the observations among many models. They obtained V_S=3.517 km/s for the averaged J-wave speed. Subsequently, normal modes were also used to invert the rigidity of the IC when forming the Preliminary Reference Earth Model (PREM) (Dziewoński and Anderson 1981). They determined V_S=3.5 km/s at the ICB with a slight increase to 3.67 km/s at the IC's center. They were later reviewed by Masters and Shearer (1990), who found the mean V_S=3.45±0.1 km/s. In conclusion, it is astonishing that normal modes can be used to probe the IC, given that this region is less than 1% of Earth's interior and mode amplitudes vanish at the center.

2.3. Body Wave Studies

Unlike normal modes, whose motions sample the entire volume of the Earth simultaneously, body wave motion can be visualized in a high-frequency approximation using rays (Figure 3A). The simplest manifestation of the IC shear-wave energy would come in the form of PKJKP waves. In PKJKP, converted compressional- to shear-wave energy is labeled with the central letter "J" to be distinct from the purely compressional body waves labeled PKIKP, with the letter "I" standing for the IC compressional waves. Other examples of body waves traversing the IC as shear waves are pPKJKP, SKJKS, and SKJKP (Figure 3A).

Generally speaking, the shear waves in the IC (J waves) suffer from the ineffective conversion between the shear and compressional energy at the ICB, thus significantly decreasing J waves' amplitudes for a range of epicentral distances. For example, theoretical studies suggest that the PKJKP may only be

214 visible in the range 130°-155°, and even in this range, the PKJKP amplitude is about one-fifth of the
215 PKIKP amplitude (Bullen 1951), which falls under the observational threshold. Furthermore, the
216 relatively small PKJKP amplitude can be even weaker due to the high attenuation structure in the IC
217 (Doornbos 1974). Last but not least, IC anisotropy can split the J waves, thereby spreading the energy
218 out in time and reducing the amplitude, as energy is shared across two interfering quasi-S waves on
219 any component of mooring. Combined, these effects make PKJKP extremely faint. Another difficulty
220 in searching for PKJKP is the unknown shear-wave speed in the IC. Theoretical travel-time curves can
221 vary quite significantly for different assumptions of IC shear-wave speed, as Figure 2 demonstrates.
222
223 Nevertheless, a few J-wave observations have been reported starting from the early 1970s (Figure 1).
224 Julian et al. (1972) identified PKJKP phases for five earthquakes (M_b>6.0) by vespagram analysis
225 using records of the Large Aperture Seismic Array (LASA). They inferred V_s= 2.95±0.1 km/s in the
226 IC. This low value disagrees with normal-mode estimates and later estimates from J-wave
227 observations (Figure 2). Okal and Cansi (1998) identified PKJKP in linearly stacked seismograms in
228 periods of 2-10 s using records at eight stations in France for June 17, 1996, deep Flores Sea earthquake
229 (H=584 km, Mw=7.9). Based on these observations, they estimated V_s=3.65 km/s. They also suggested
230 that the disagreement can be reconciled if the observations by Julian et al. (1972) are re-interpreted as
231 pPKJKP. Deuss et al. (2000) observed pPKJKP and SKJKP in stacked seismograms at periods 10-100
232 s for the same event with 47 global stations and the phase-weighted stacking (PWS) method. They
233 estimated V_s= 3.6 km/s.
234
235 Cao et al. (2005) observed PKJKP in stacked seismic recordings in 10-17 s from the Grafenberg
236 Seismic Array in Germany for 1999, Melanesia (H=76 km, Mw=7.3), earthquake using the PWS
237 method. They obtained similar V_s from PKJKP observations, however, they suggested a ~1.5%
238 increase of V_s in the IC relative to PREM. They argued that the increase is due to different depth-

239 dependent sensitivities of normal modes and PKJKP to V_s, where the modes mainly sample the shallow
240 parts of the IC while the PKJKP traverse the IC near its center. Using short-period records at the Hi-
241 Net array for a 2006 earthquake in Mozambique (11 km deep, M7.0), Wookey and Helffrich (2008)
242 detected PKJKP in periods of 2-20 s. Waszek and Deuss (2015) also present unconfirmed observations
243 of J waves by examining a few earthquakes.
244
245 It is worth noting that apart from shear waves directly sensitive to the IC shear modulus (and shear-
246 wave speed), compressional waves are also susceptible to the shear modulus at the top of the IC, near
247 the ICB. A good example is the seismic phase PKIIKP (Cormier 2015; Krasnoshchekov et al. 2019),
248 reflecting from the lower side of the ICB. Figure 3A shows these seismic body waves and their ray
249 paths in high-frequency approximation. Krasnoshchekov et al. (2019) suggested relatively low V_s, in
250 the range of 1.5-3 km/s, at the top of the IC by analyzing the PKIIKP amplitude. They proposed that a
251 mosaic-like surface of the IC could explain the observed V_s reduction and significant V_s variations in
252 their study.
253

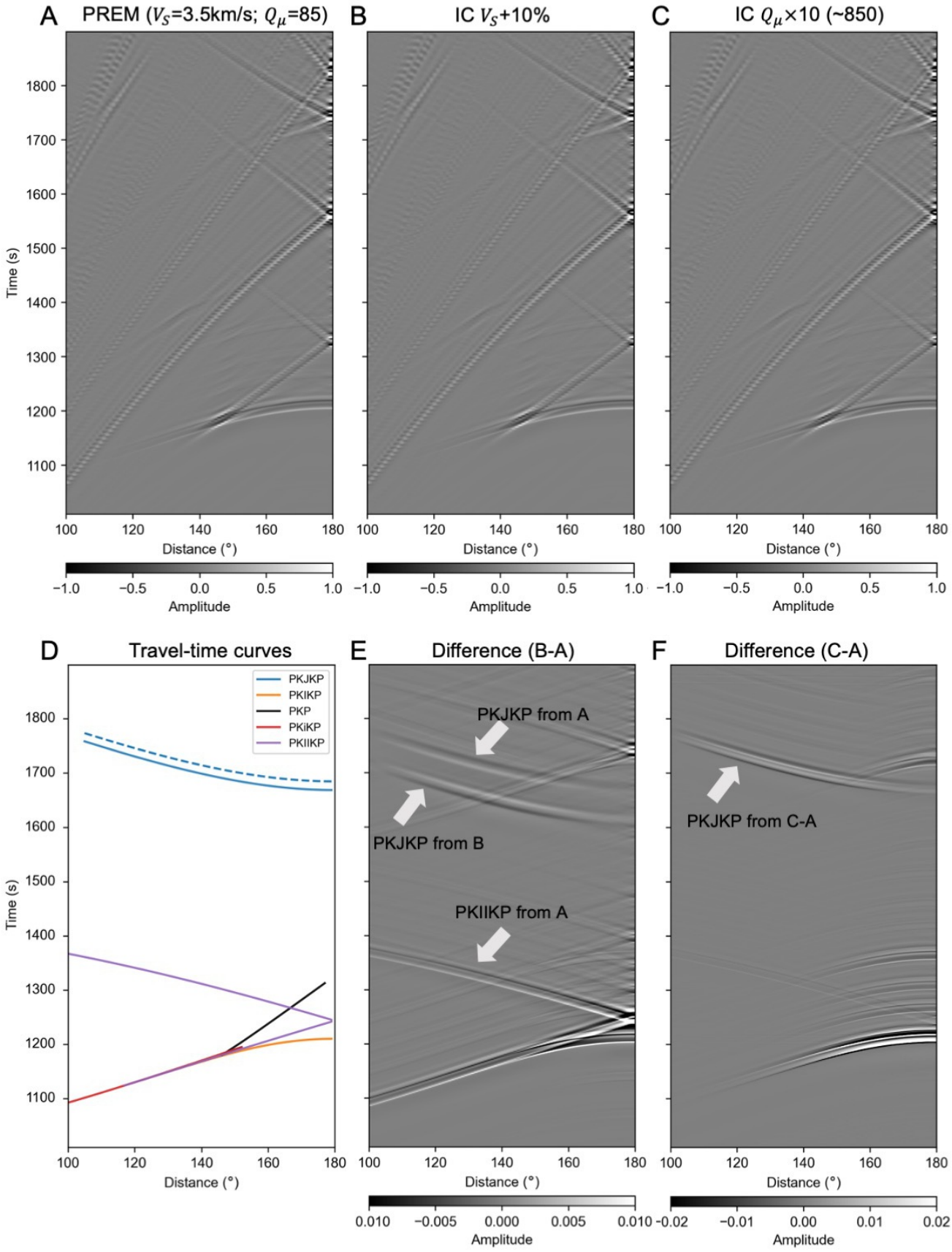
A
PREM (V_S=3.5km/s; Q_μ=85)
B
IC V_S+10%
C
IC Q_μ×10 (~850)
Time (s)
Distance (°)
Amplitude
D
Travel-time curves
PKJKP
PKIKP
PKP
PKiKP
PKIIKP
E
Difference (B-A)
PKJKP from A
PKJKP from B
PKIIKP from A
F
Difference (C-A)
PKJKP from C-A

Figure 4

Synthetic wavefields for seismic body waves sensitive to the solid IC. (A) Synthetic wavefield from the PREM reference model. (B) Synthetic wavefield from an Earth model with 10% increase in IC shear wave (J-wave) speed relative to PREM. (C) Synthetic wavefield from an Earth model with the IC's Q_μ increased by ten times relative to PREM. (D) Theoretical travel-time curves (solid lines) for some relevant seismic phases sensitive to the IC based on (A). Dashed line for PKJKP waves corresponds to the updated PREM model in the IC for shear-wave speed according to Tkalčić & Phạm (2018). (E) Wavefield difference between (B) and (A). (F) Wavefield difference between (C) and (A). Yspec simulation software (Al-Attar & Woodhouse 2008) was used to produce synthetic wavefields.

Shearer et al. (2011) investigated possible causes behind the difficulties associated with observing reliable PKJKP waves and demonstrated that routine observations are extremely unlikely at periods longer than 10 s. As shown in Figure 4, we produce the synthetic seismic wavefield by revisiting the analysis of Shearer et al. (2011). The synthetic wavefield, calculated using the PREM model (Figure 4A), and the synthetic wavefields calculated by increasing the IC's Vs by 10% (Figure 4B) and multiplying Q_μ by 10 (Figure 4C), remain visually invariant. PKJKP is not visible as more prominent mantle waves dominate it. Thus, considering the results of Shearer et al. (2011), the only way to make PKJKP visible is by taking the difference between synthetic wavefields generated using different IC shear properties (Figures 4D and 4E). Sections 3 and 5 contain more discussion on shear attenuation. To explain most published J-wave observations, Shearer et al. (2011) argued that they must result from exceptional focusing effects or a less-attenuative IC than current models predict. Thus, due to the challenging observing conditions, but because J waves would provide invaluable constraints on IC property puzzles, they are referred to as "The Holy Grail" of modern global seismology (Shearer 2009).

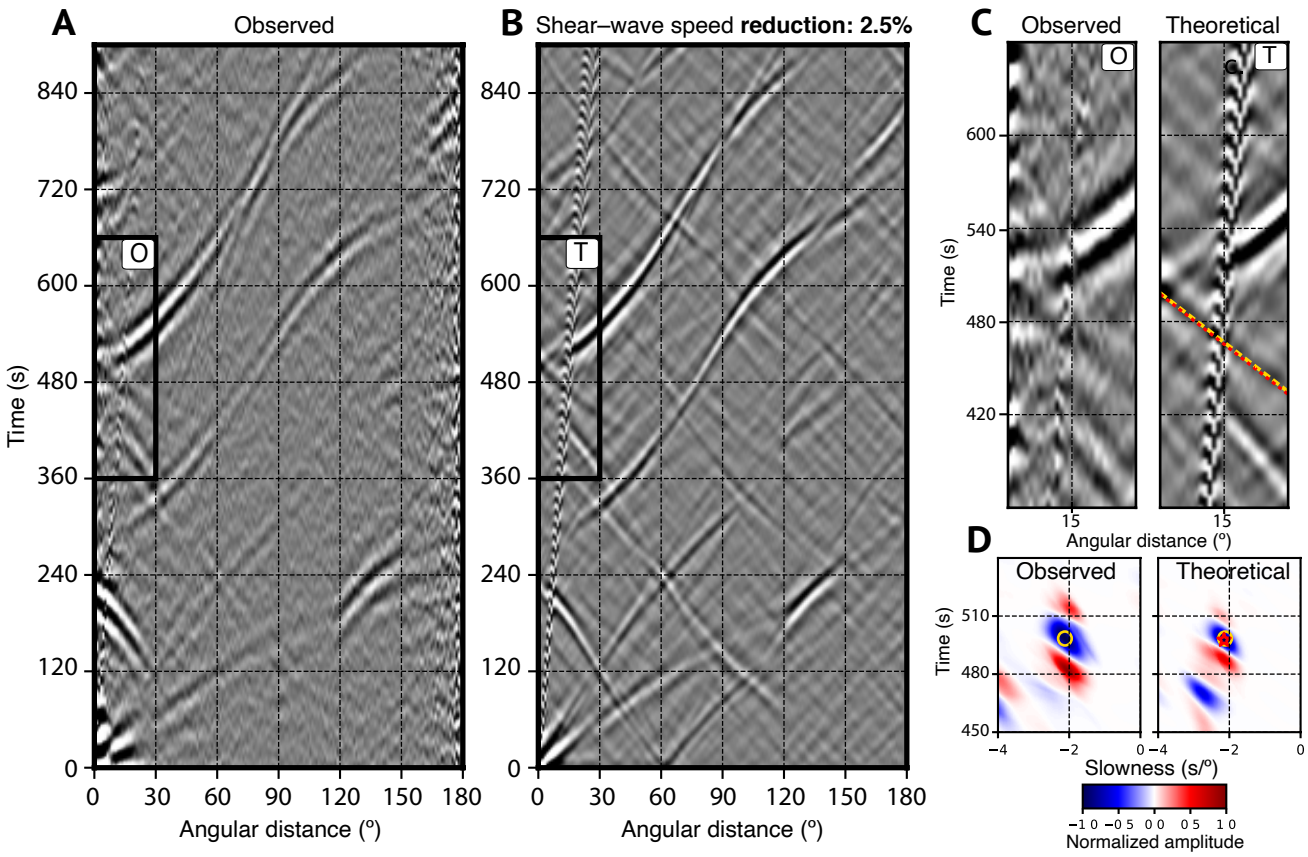

Figure 5

Observed and synthetic correlograms and the I2-J cusp. A comparison between (A) the observed Earth's cross-correlogram and (B) the best-fit simulated Earth's cross-correlogram for the central period of 23.1 s. The best-fit simulation uses the PREM model with the IC shear-wave speed reduced by 2.5%. (C) Enlargements of windows O (observed) and T (theoretical), focused on the I2-J cusp. (D) The observed and simulated (theoretical) slant-stacks with the yellow circle corresponding to the lower branch of the I2-J cusp in the slowness-time domain and the yellow dotted line corresponding to the same in the travel-time domain. The red star and red dotted line are the values based on the best-fit Earth model with the 2.5% reduction of shear-wave speed in the inner core. Reproduced from Tkalčić & Phạm (2018).

2.4. Coda-Correlation Studies

A new method to observe IC shear wave energy has recently come to light from the earthquake coda-correlation studies (for a recent review, see Tkalčić et al. 2020). Notably, the similarity between the two weak signals in the late earthquake coda becomes more prominent than the weak signals themselves. J waves manifested themselves via their similarity with other seismic core phases in the

296 coda-correlation wavefield (Tkalčić & Phạm 2018). Specifically, a pair of seismic phases
297 (xPKIKPPKIKP-xPKJKP), with similar slowness, and hence, waveforms, can result in a cross-
298 correlation peak and the feature named I2-J. The "x" represents any seismic phase (Figure 3B and 3C).
299 For example, "x" can be replaced with PcP, and as a result, the pair that contributes to the formation
300 of I2-J becomes (PcPPKIKPPKIKP-PcPPKJKP). Similarly, for x=PKIKP, the pair of phases
301 contributing to the formation of I2-J becomes (PKIKPPKIKPPKIKP-PKIKPPKJKP). In reality, for
302 the late earthquake coda, i.e., 3–10 hours after origin time (Phạm et al., 2018), the prefix "x" can
303 correspond to a complicated combination of ray multiples because of a diverse propagation of seismic
304 waves possible in such a long time. All of them can contribute to I2-J.
305
306 When all contributions described above are stacked, the I2-J amplitude is enhanced and becomes
307 visible in a global correlogram. As shown in Figure 5, the I2-J is identified as a cusp of energy in the
308 synthetic correlogram whose timing was shown as dependent on IC shear-wave speed (shown in Figure
309 2 in Tkalčić & Phạm (2018)) and could be compared with the observed correlogram. This dependency
310 presents a novel type of observation of the J wave and a new method to investigate shear wave
311 properties in the IC. Tkalčić & Phạm (2018) obtained evidence for a solid, but a "soft" (high Poisson
312 ratio) Earth's inner core, with shear-wave speeds and shear moduli of 3.42±0.02 km/s and 149.0±1.6
313 GPa near the inner core boundary and 3.58±0.02 km/s and 167.4±1.6 GPa in the Earth's center, the
314 values that are 2.5% lower than those reported in PREM (Dziewoński & Anderson 1981).
315
316 Interestingly, all the J-wave speed estimates from seismological observations, as summarized above,
317 are overall lower than V_s estimates from mineralogical experiments (e.g., Antonangeli et al. 2004; Mao
318 et al. 1998; Vočadlo 2007). The iron or its alloy at the IC pressure and temperature conditions exhibits
319 much larger V_s than the values estimated from the seismological observations. To explain such a
320 significant discrepancy, different IC models have been suggested. Among the proposed models are:
321 the presence of low-velocity components or anelastic effects in the IC (Mao et al. 1998), partial melting

322 that results in liquid in the IC (Singh et al. 2000; Antonangeli et al. 2004; Vočadlo 2007), the presence
323 of different solid iron phase or existence of light elements or anharmonic high-temperature effects
324 (Antonangeli et al. 2004), and imperfect iron crystals including the grain boundaries and defects
325 (Belonoshko et al. 2007).
326
327
328 ## 3. SHEAR ATTENUATION IN THE INNER CORE
329 Intrinsic attenuation in shear is a property that measures energy loss per cycle of the shear wave
330 propagating through Earth's inner core (for a recent review on attenuation, see Cormier, 2020). This
331 quantity provides critical constraints on the thermal states, viscosity, and stable crystallographic
332 structure of iron in the IC (e.g., Belonoshko et al., 2019). Similar to the shear-wave speed counterpart,
333 early constraints on shear attenuation came from normal modes, which were later followed by a few
334 claimed observations of PKJKP body waves. However, the level of disagreement among reported
335 attenuation estimates in shear is significantly greater than for shear-wave speeds presented in Section
336 2. Recently, the advancement in the theoretical understanding of the correlation wavefield holds great
337 potential to provide independent constraint on the shear attenuation properties and is worth exploring
338 in near future research.
339

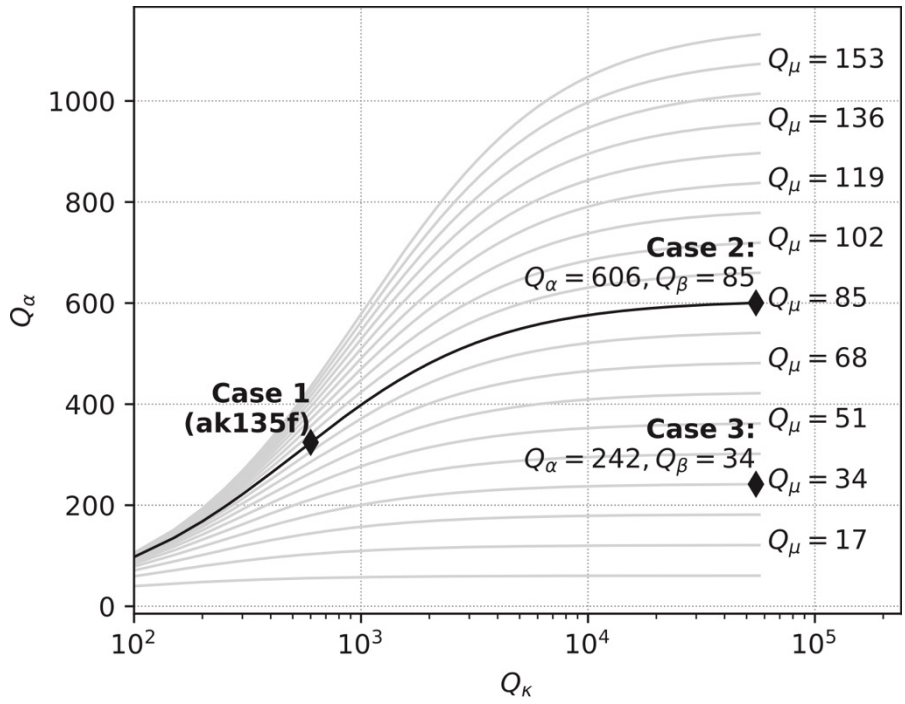

Figure 6

Graphical illustration for the relation of compressional-wave quality factor (Q_α) as a function of bulk (Q_κ) and shear quality factors (Q_μ) according to Equation (4). The diamonds mark the set of values used to compute synthetic waveforms shown in Figure 10 and Figure 11 in the last section. The thick line represents the IC Q_α value from the PREM model (Dziewoński & Anderson 1981).

Q is a quality factor defined as the average energy W divided by the loss of energy per cycle ΔW, $Q = W/\Delta W$. Note that Q is inversely proportional to the energy loss, so higher Q means the material is less attenuative. In a solid material, elastic energy is dissipated in bulk and shear oscillations, denoted by Q_κ and Q_μ. Attenuation of compressional (Q_P^{-1}) and shear waves (Q_S^{-1}) can then be expressed as (Anderson & Hart, 1978):

$$Q_P^{-1} = L\,Q_\mu^{-1} + (1-L)Q_\kappa^{-1}\ ;\ Q_S^{-1} = Q_\mu^{-1}, \tag{4}$$

where $L = 4{V_S}^2/3V_P^2$. This relation is graphically illustrated in Figure 6. It is worth noting that attenuation in shear, Q_μ^{-1}, is identical to shear-wave attenuation, Q_S^{-1}, while compressional-wave

355 attenuation, Q_P^{-1}, depends on both bulk and shear attenuation. For each value of the shear quality-
356 factor, Q_μ (indicated on the right column), Q_P increases monotonously as a function of Q_κ. When Q_κ
357 approaches infinity, Q_P approaches its upper limit, Q_μ/L. Thus, compressional-wave attenuation can
358 be used as a proxy to constrain attenuation in shear. The observed Q might be different at normal
359 mode than body-wave frequencies and spatial scales. The readers are referred to other review texts
360 (e.g., Romanowicz and Mitchell, 2015; Souriau and Calvet, 2015; Tkalčić, 2017).
361
362 Normal-mode studies rely on amplitudes of IC modes sensitive to attenuation in shear at periods of
363 ~100 s and longer. Some studies suggested large values, namely Q_μ>1000 (Masters and Gilbert, 1981;
364 Suda and Fukao, 1990) based on anomalously high amplitudes of some modes, e.g., ${}_6S_2$, ${}_7S_3$. However,
365 those modes were later found to be possibly misidentified (Widmer et al., 1991), and normal-mode
366 studies settled to more attenuative IC models (i.e., smaller Q_μ values) later. In PREM (Dziewoński and
367 Anderson, 1981) Q_μ was set to 84, and Widmer et al. (1991) found Q_μ=110 when the possibly
368 misidentified modes were excluded. The shear-quality factors similar to PREM ($Q_\mu \cong 84$) were later
369 confirmed by Resovsky et al. (2005) and de Wit et al. (2014) when they employed inversion schemes
370 with robust accounts for uncertainty. Most recently, Talavera-Soza and Deuss (2020) investigated the
371 spherical mode couple ${}_{10}S_2 - {}_{11}S_2$ and considered the trade-off between attenuation in shear and shear-
372 wave speed, as well as the mode-coupling effect (Andrews et al., 2006). They found a similar value
373 for shear attenuation quality-factor as in PREM (i.e., $Q_\mu = 84$) with either a reduction of 0.5% in the
374 IC shear-wave speed or an increase of IC radius by 0.5%. The accepted values for shear attenuation
375 quality-factor (~84–110) suggests that the Earth's IC is possibly the most attenuative volume in the
376 Earth.
377
378 However, strong attenuation in shear (i.e., low Q_μ) is not favorable for any observations of body waves
379 propagating as shear waves in the IC (Doornbos, 1974). Thus, a few claimed observations of J waves,

made using the waveforms bandpass-filtered at relatively short periods, concluded possible higher Q_μ, at least along specific corridors through the IC. In the period ranges 10–100 seconds, Deuss et al. (2000) estimated $Q_\mu = 120$ from the observation of pPKJKP and SKJKP waves. Cao and Romanowicz (2009) extended their observation of PKJKP made earlier (Cao et al. 2005) for a similar period range and estimated $Q_\mu = 315$ from the observed PKJKP waves. Both studies noted significant challenges in observing J waves, even in the synthetic waveforms. Cao and Romanowicz (2009) compared the observed with the synthetic waveforms where the solid-IC synthetics were subtracted from the liquid-IC synthetics (an operation somewhat similar to the one shown in Figure 4). Wookey and Helffrich (2008) observed PKJKP at shorter periods, 2–20 s, and indicated that their observation required $Q_\mu = 200$ at the top 400 km of the IC but had no sensitivity to constrain shear attenuation at greater depths.

A simple explanation for different values of attenuation quality-factors obtained from normal-mode and body-wave studies is due to the frequency-dependent nature of attenuation. Alternately, it could be due to the variation of attenuation as a function of depth in the IC, since normal modes are mainly sensitive to the IC top, while the J waves penetrate deeper in the IC. However, due to the sparsity of reliable observations, a reconciliation of the two types of studies is still at the forefront of research in this field.

Recently, Tkalčić and Phạm (2018) presented an initial attempt to constrain the shear attenuation with the detection of J waves' footprint in the global correlation wavefield. Their fit of the I2-J amplitudes to the synthetized features requires a 75% reduction relative to the PREM value. This significant reduction would indicate an even more substantial attenuation in shear than current values inferred from the normal-mode studies indicate. However, the authors acknowledged that the method of estimating Q_μ was possibly over-simplified as many factors that could impact the resultant amplitudes

404 in the correlation wavefield were excluded from consideration. A further extension of that experiment
405 is presented in Section 5, hoping to provide useful directions for future research.
406
407 ## 4. SHEAR-WAVE ANISOTROPY IN THE INNER CORE
408 Anisotropy in shear-wave speed has been hypothesized to exist in conjunction with the observed
409 anisotropy in compressional-wave speed, but the observations to confirm this hypothesis have been
410 elusive. It was noticed that the compressional waves traverse the IC faster in directions quasi-parallel
411 to the Earth's rotation axis than in directions quasi-parallel to the equator (e.g., Poupinet et al. 1983;
412 Morelli et al., 1986; Woodhouse et al., 1986). The anisotropy for both compressional and shear waves
413 reflects preferred alignments of iron crystal formed either during the formation of the IC (Karato 1993;
414 Bergman 1997) or its post-formation dynamics. i.e., recrystallization and plastic deformation (Yoshida
415 et al. 1996; Karato 1999; Wenk et al. 2000a; Buffett et al. 2001) or the convection in the viscous IC
416 (Jeanloz & Wenk 1988; Wenk et al. 2000b). Regarding the crystallographic structure of iron-nickel
417 alloy stable under the IC conditions, it is uncertain whether it is hexagonal-close-packed (hcp) (e.g.,
418 Stixrude & Cohen, 1995; Mao et al. 2006; Fischer & Campbell 2015; Steinle-Neumann et al., 2001)
419 or body-centered-cubic (bcc) structure (Vočadlo et al., 2003; Belonoshko et al., 2008; Calvet &
420 Margerin, 2008). For this reason, the constraints on IC shear-wave anisotropy can complement studies
421 of IC compressional-wave anisotropy and further improve our understanding of the IC material
422 rheology (e.g., Karato, 2008) and its dynamics (e.g., Sumita & Bergman 2015).
423
424 We can expect two phenomena for shear-wave anisotropy in theory: direction-dependent speed
425 variations and shear-wave splitting into two polarized shear waves propagating at a different speed.
426 For a cylindrically anisotropic (or transversely isotropic) medium such as the one hypothesized for the
427 IC, its elasticity tensor C_{ij} can be described by five independent constants: C_{11}, C_{33}, C_{44}, C_{12}, C_{13}:

$$C_{ij} = \begin{bmatrix} C_{11} & C_{12} & C_{13} & & & \\ C_{12} & C_{11} & C_{13} & & & \\ C_{13} & C_{13} & C_{33} & & & \\ & & & C_{44} & & \\ & & & & C_{44} & \\ & & & & & \frac{(C_{11}-C_{12})}{2} \end{bmatrix}. \quad (5)$$

Based on low-order harmonics approximations (Backus 1965; Crampin 1977), we can derive the seismic-wave speed:

$$\rho V_{S1}^2 = C_{44}(sin^4\xi + cos^4\xi) + (C_{11} + C_{33} - 2C_{44} - 2C_{13})sin^2\xi cos^2\xi, \quad (6)$$

$$\rho V_{S2}^2 = \frac{(C_{11}-C_{12})}{2} sin^2\xi + C_{44}cos^2\xi, \quad (7)$$

$$\rho V_P^2 = C_{11}sin^4\xi + C_{33}cos^4\xi + (4C_{44} + 2C_{13})sin^2\xi cos^2\xi, \quad (8)$$

where V_{S1} and V_{S2} are the speeds for split shear waves with polarization parallel to meridians and the equator, respectively, V_P the compressional wave speed, ρ the density, and ξ the angle between J-wave ray paths and the Earth's rotation axis. Figure 7 showcases V_{S1} and V_{S2} for the two split shear waves and their variations with the ξ by taking elastic constants for simple IC models made of hcp- or bcc-iron following Mattesini et al. (2010). If observed for J waves, such phenomena would be direct evidence for shear-wave anisotropy in the IC.

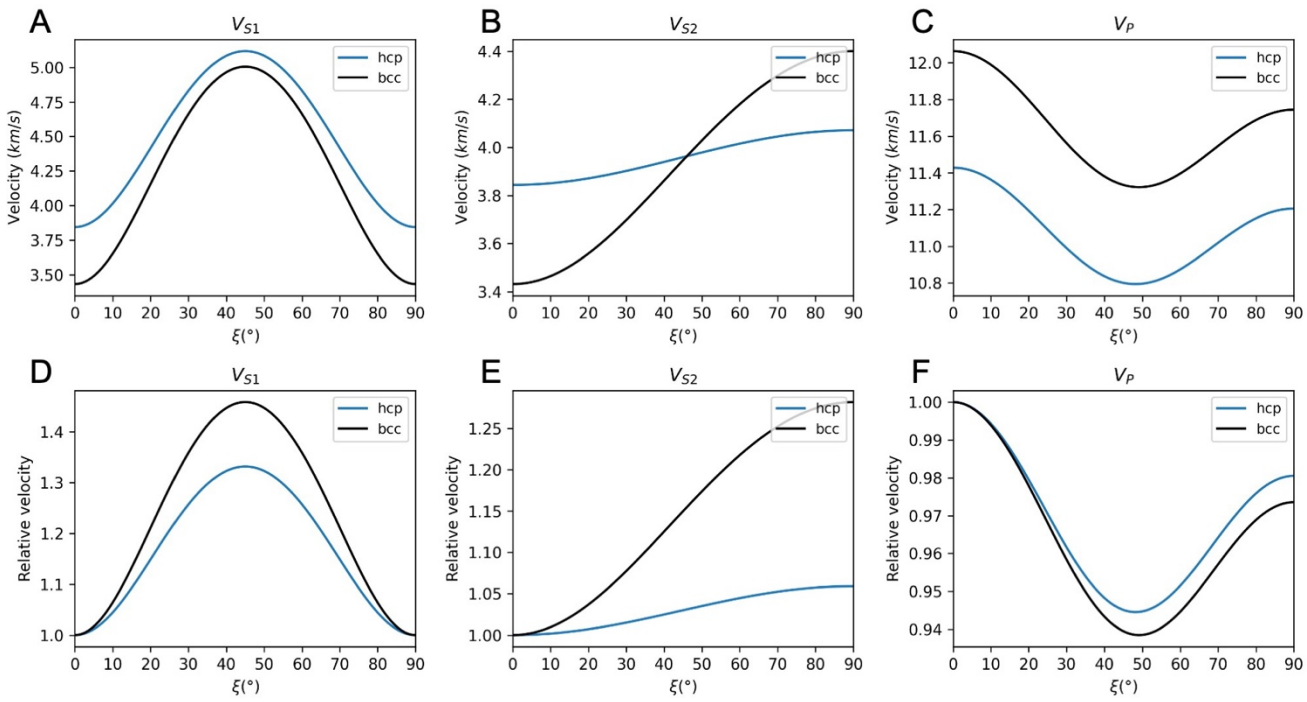

445

446 Figure 7

447 Theoretical predictions for anisotropy in shear- and compressional-wave velocity for simple IC models
448 made of hcp- (blue lines) or bcc-iron (black lines). (A) Velocity variations for compressional wave
449 relative to the angle ξ, the angle between a seismic wave ray-path and the Earth's rotation axis. (B, C)
450 Velocity variations for shear waves with polarization parallel to meridians and the equator,
451 respectively. (D, E, F) Variations for relative velocities corresponding to A, B, and C, respectively.
452 The velocities are calculated based on Equations (5-8) with elastic constants taken from Mattesini et
453 al. (2010).

454

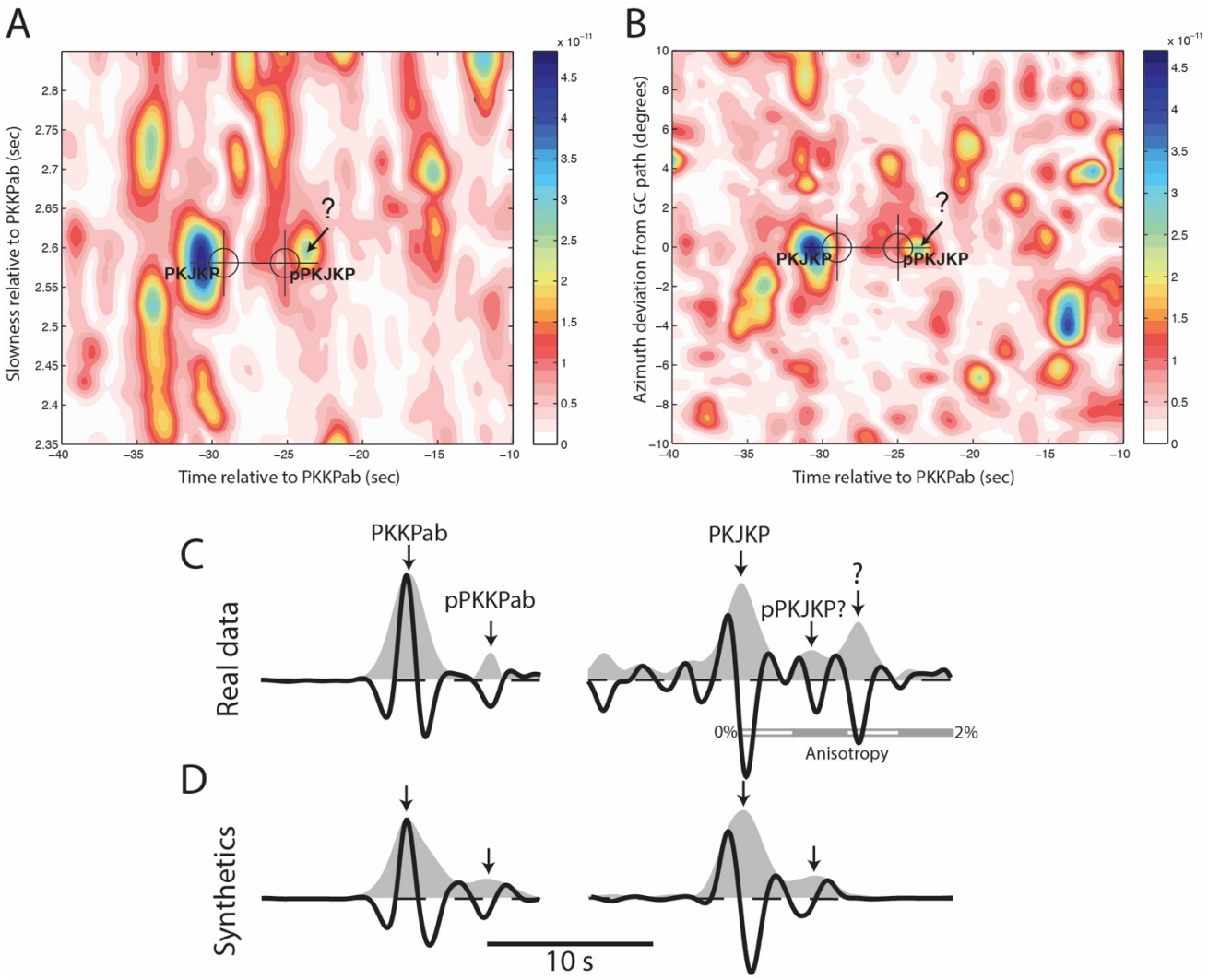

Figure 8

Observations of PKJKP waves and IC shear-wave anisotropy. (A) Time-slowness "slant stacks" for detecting PKJKP. The crosses indicate the theoretical predictions for PKJKP and pPKJKP arrivals. The energy maxima close to the predictions are identified as PKJKP and pPKJKP arrivals. The observed time of PKJKP is ~1.5 s before the prediction and at the correct slowness within the array's resolution (~0.05 s/°). The pPKJKP's amplitude is near the noise level (denoted by the question mark). (B) Azimuthal slant stack at a fixed slowness of 2.6 s/°. The energy maximum identified as PKJKP arrival is within 0.2° of the (major arc) great-circle path (this means that the observed energy arrives from the earthquake as predicted, along the great-circle). The second energy peak is close to the pPKJKP prediction (denoted by the question mark). (C, D) The observed and synthetic waveforms, respectively. The waveforms are phase-weighted slant stacks at the peak slowness for PKKPab and PKJKP. The shaded area is the waveform envelope. The observations and synthetics are matched well for PKKPab, pPKKPab, PKJKP, and pPKJKP arrivals, as labeled. The arrival denoted by the question mark is possibly the split J-wave due to IC anisotropy. The scale bar shows the time-lag predictions

for an IC anisotropy model, implying that a 1% shear-wave anisotropy can explain the split. Reproduced from Wookey and Helffrich (2008).

If the J waves are characterized as elusive due to rare observations, evidence for shear-wave anisotropy is even more elusive. The first evidence for shear-wave anisotropy was reported by Wookey and Helffrich (2008). The authors observed a seismic arrival ~7 s after the main PKJKP arrival (or ~3 s after pPKJKP) using the Hi-net array data (Figure 8). They eliminated the possibility of the arrival being the source-side converted phase, such as sPKJKP, as the accompanying phases do not exist for more pronounced PKKPab and PKiKP waves arrivals. The newly observed conspicuous arrival was then interpreted as the result of shear-wave splitting in the IC and evidence for J-wave anisotropy. The anisotropy strength was estimated at ~1% for the waveforms in the period range 2–20 s averaged for the whole J-wave ray path from the time difference between two split J waves.

Furthermore, based on the quantitative evaluation of J-wave anisotropy, Wookey and Helffrich (2008) explored a range of iron structure models that represent a series of orientations and rotational averages of hcp and bcc iron. Multiple models yield similar J-wave anisotropy that is comparable to the observation. Among those models, Wookey and Helffrich (2008) preferred an hcp model with its *c* axis (the axisymmetric axis) parallel to Earth's equator, based on the IC compressional-wave anisotropy constraints. The model exhibits faster P-waves in the directions perpendicular to the *c* axis as predicted in mineralogical experiments (e.g., Steinle-Neumann et al. 2001). However, for the same model, different experiments (e.g., Stixrude & Cohen 1995; Antonangeli et al., 2006; Vočadlo et al., 2009) reported quite the opposite sense of compressional-wave anisotropy, i.e., that the P-waves are faster along the *c* axis (e.g., Antonangeli et al., 2006; Vočadlo et al., 2009).

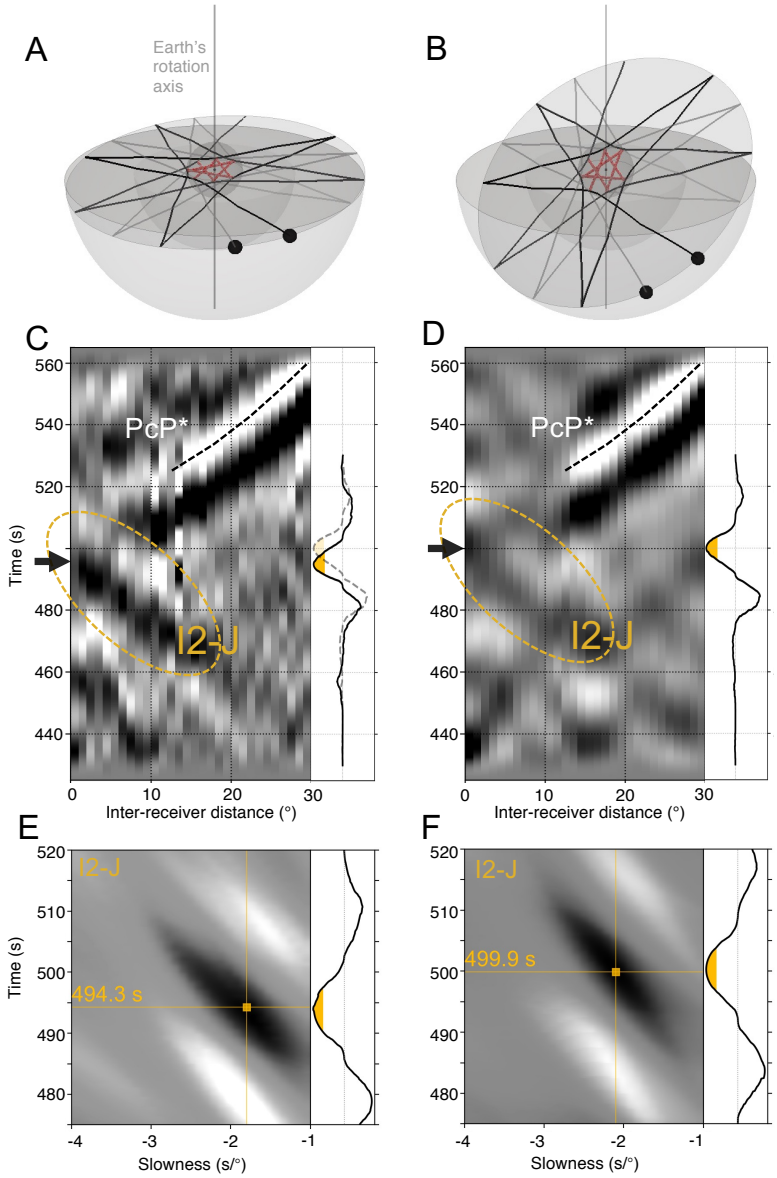

Figure 9

IC shear-wave anisotropy observations from earthquake coda-correlation. (A) Geometry settings for the coda-correlation feature I2-J for two receivers (black balls) close to the equator. Red lines represent J waves, and black and grey lines represent compressional waves. The constituents of I2-J are multiples that consist of a set of common rays, as shown in Figures 3B and 3C. All the J waves (shown in red) are in directions parallel to the equator. (B) Similar to (A) but for receivers in a plane oblique to the equator. The J-wave directions are now parallel or oblique to the equator. (C, D) Coda-correlograms corresponding to (A) and (B), respectively. Yellow ellipses and black arrows indicate I2-J. The dash lines indicate the referent feature PcP*. (E, F) Slant stacks of I2-J for the two correlograms in (C) and (D), respectively. The yellow dots correspond to the lower branch of the I2-J cusp. Each slant stack is

506 normalized relative to the maximal amplitude. The I2-J waveform stacks are shown alongside the slant
507 stacks and the correlograms. Reproduced from Wang and Tkalčić (2021).
508
509 Recently, Wang and Tkalčić (2021) have reported, for the first time, J-wave anisotropy from
510 earthquake coda-correlation observations. The rationale behind the study is that the coda-correlation
511 feature I2-J, sensitive to J-wave speed (Tkalčić & Phạm 2018), exhibits time and amplitude variations
512 when the contributing J waves sample the IC in different directions (Figure 9A, B). It was concluded
513 that J-wave anisotropy in the IC is the simplest and a plausible explanation for the observed time
514 variation. Furthermore, the reduced amplitude of I2-J formed by J waves sampling the IC in diverse
515 directions relative to the Earth's rotation axis point to J-wave anisotropy. Those J waves can have a
516 significant time difference (up to tens of seconds) as predicted for cylindrical anisotropy in the IC (e.g.,
517 Stixrude & Cohen, 1995; Song, 1997; Vočadlo et al., 2009). Such time difference can result in
518 destructive stacking and hence decrease the amplitude of I2-J (Wang and Tkalčić 2020). From the new
519 class of observations, Wang and Tkalčić (2021) estimated that shear waves traversing the IC near its
520 center travel faster for the oblique than for the equatorial angles relative to the Earth's rotation axis by
521 at least ~5 s (Figure 9C, D, E, F) in the period range 15-50 s. This time difference corresponds to a
522 cylindrical anisotropy strength of at least ~0.8%. The current state-of-the-art correlation-wavefield
523 data processing does not allow us to isolate individual J waves for I2-J. Hence, the anisotropy strength
524 cannot be quantified with better accuracy. For the same reason, J-wave splitting cannot be observed
525 from coda-correlation stacks, and the derived J-wave observations correspond to an average of two
526 split J waves.
527
528 Based on the J-wave anisotropy observations, Wang and Tkalčić (2021) took a step further to verify
529 the compatibility of various iron crystallographic models. They were able to rule out one incompatible
530 model of crystallographic state of iron for the IC. They examined different hcp- and bcc-iron models
531 with varying crystal alignments, assuming a single crystal for the whole IC. Among the candidate

models, a bcc model with <001> axis (the cube edge) parallel to the Earth's rotation axis predicts opposite anisotropy to the observation. Hence, it can be excluded from candidate IC iron models. In contrast, predictions for other hcp and bcc models agree with the observation, but they are indistinguishable because they exhibit similar anisotropy.

Both the analyses by Wookey and Helffrich (2008) and Wang and Tkalčić (2021) rely on elastic properties for different iron models. The elastic properties can be simulated for hcp- and bcc-iron at the IC's high-pressure and high-temperature conditions (e.g., Mao et al. 2006; Belonoshko et al. 2008; Vočadlo et al., 2009; Fischer & Campbell 2015). The shear-wave anisotropy can be computed based on Equations (5–7) with the simulated elastic moduli. Apart from that, the shear-wave anisotropy can be obtained for iron crystals in high-pressure and high-temperature experiments. Lin et al. (2010) inferred shear-wave anisotropy for hcp-iron at high pressures and room temperature using nuclear resonant inelastic X-ray scattering technique. The results show that the shear waves are 2-4% faster in directions parallel to the *c* axis than directions perpendicular to the *c* axis at 158 GPa and 172 GPa. However, technical difficulties remain in measuring reliable shear-wave speed for iron crystals related to finite-strain theory and iso-stress assumptions used in the modeling, and the strong influence of plastic deformation of the crystals (Antonangeli et al.; 2006 Lin et al. 2010).

5. CHALLENGES, FUTURE DIRECTIONS AND NEW OBSERVATIONS

The biggest challenges in studying the shear properties of the IC have been in observing the IC-sensitive shear waves (J waves) and correctly identifying and quantifying Earth's normal modes sensitive to the IC shear structure. In the former case, the J waves are sufficiently weak to lie under the observational threshold of noise. The uncertain travel-time prediction makes their observations highly challenging and quite a different kind of exercise from routine observations of other seismic phases. In the latter case, advances in normal-mode theory and deep Earth-imaging gradually enabled

558 a better command of the observed IC shear structure-sensitive normal modes. In both cases, the
559 technological advances in seismometer construction increased the quality of data. Their proliferation
560 worldwide, including remote areas and the ocean floor, enable unprecedented accumulation of digital
561 data. Last but not least, most recent new approaches to data analyses, considering the information
562 contained in the data that once was considered noise, enabled considerable progress. Here, we will
563 consider two research directions that hold the potential of increasing our observational constraints on
564 IC attenuation in shear and IC shear-wave speed.
565
566 **5.1. Characterizing IC's attenuation in shear using the global correlation wavefield**
567 To complement constraints from body waves and normal modes to look into the shear properties of
568 the IC, global seismologists have recently explored the late earthquake-coda correlation that exploits
569 the similarity of seismic waveforms. This review has featured the work in which J waves were
570 observed due to their similarity with PKIKPPKIKP (I2) waves in Earth's correlogram (Tkalčić and
571 Phạm, 2018). The correlation feature associated with J waves was dubbed I2-J in the original paper,
572 which also discussed the potential for full-waveform modeling and measuring attenuation. Here, as an
573 illustration of the way forward, we consider amplitudes of several other prominent features in Earth's
574 correlogram to constrain IC attenuation. The considered IC-sensitive features include (i) *I** – which
575 can be compared to PKIKP waves in the direct seismic wavefield, traversing the bulk of the IC, (ii)
576 *I2** – the double of *I**, traversing the bulk of Earth's IC twice, (iii) *(II)2** – equivalent to the first
577 multiple of PKIIKP, an underside ICB reflection, and (iv) *I2-J* – formed due to the similarity of *I2* and
578 *PKJKP* waveforms.

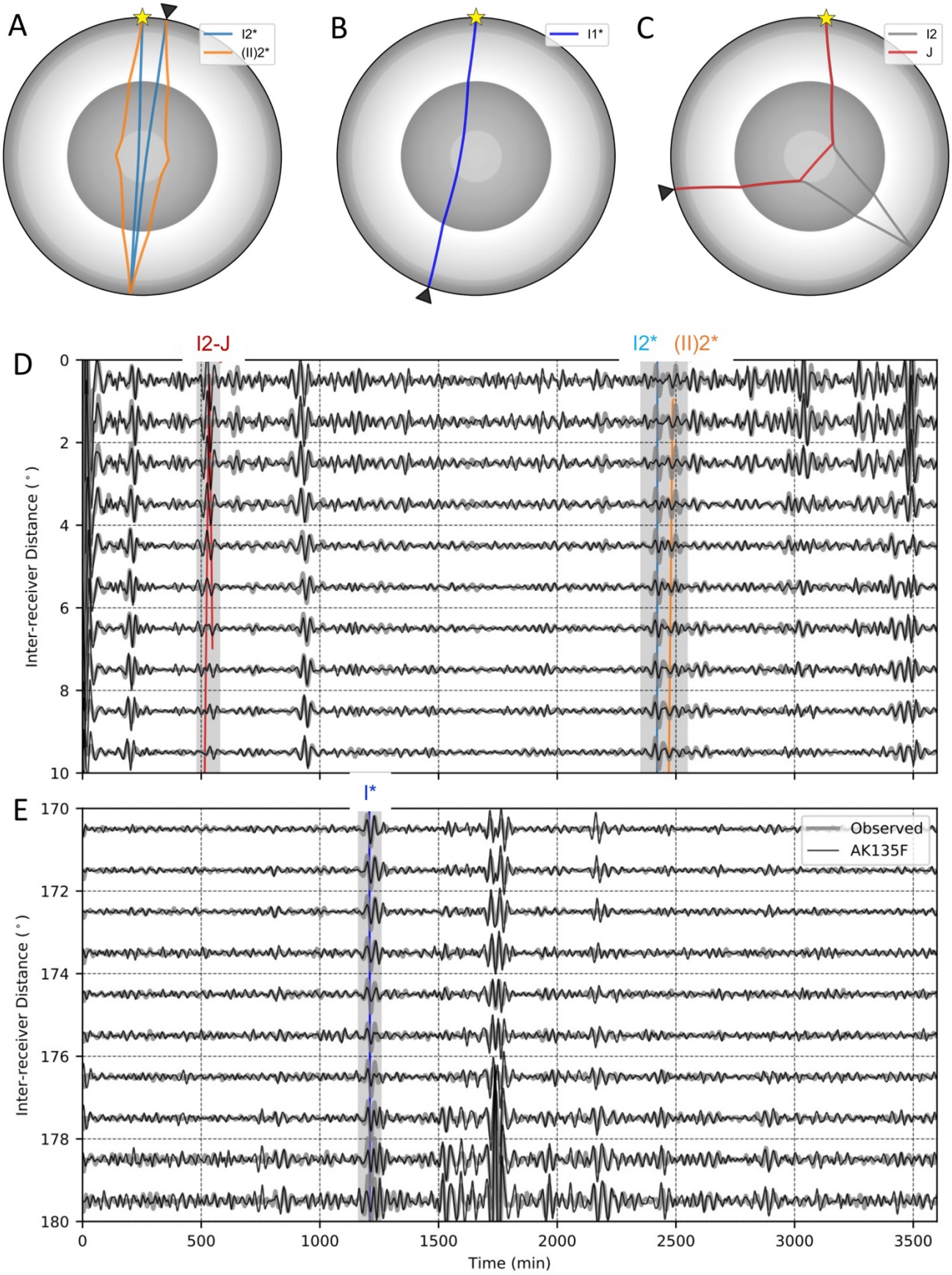

579

580 Figure 10

Ray-path geometry for IC-sensitive features under consideration, showing the common set of legs that constitute each feature. A) PKIKPPKIKP* (abbreviated as I2*) and PKIIKPPKIIKP* (abbreviated as (II)2*) at small inter-receiver distances. B) PKIKP* (abbreviated as I*) at near antipodal inter-receiver distances. C) I2 and PKJKP (abbreviated as J) contributing to the correlation feature I2-J at small inter-receiver distances. Comparison of the observed and synthetic correlation waveforms as a function of two different inter-receiver distance ranges: D) 0–10° and E) 170–180°. Shaded areas highlight inner-core sensitive features considered in this study. I2-J, I2*, (II)2* are observed at inter-receiver distances approaching zero, while I* are observed at near-antipodal distances.

Figures 10A-C show the ray-path geometry for the common set of legs of the considered IC-sensitive features. All features involve compressional waves traversing the IC; thus, they are sensitive to the attenuation of compressional waves, Q_P^{-1} (see Equation (4)). The amplitude of the ICB underside reflection, (II)2*, could also have a weak sensitivity to shear-wave speed near the IC top as it is influenced by the reflection/refraction of S waves interacting with the boundary (this effect for PKIIKP is shown in Figure 4E). However, the fourth feature involves a shear leg in the IC; thus, it can help constrain the attenuation of shear waves in the IC. Note that I*, I2*, and PKJKP sample the central region of the IC, while the underside reflection II(2)* are sensitive to the uppermost part of the IC. Simultaneous utilization of these four correlation features' amplitudes in a common period-band, 15–50 seconds, is expected to constrain both compressional and shear-wave attenuations jointly.

In particular, we use numerical simulations (AxiSEM: Nissen-Myer et al., 2014) to generate synthetic seismograms and construct the synthetic correlation wavefield (see Phạm et al., 2018 and Tkalčić et al., 2020 for details on the computation of the correlation wavefield). In the synthetic experiments, we employ a realistic source-receiver configuration, the published focal mechanism, and source time functions from the SCARDEC catalog (Vallée and Douet, 2016) to minimize their effect on the correlation amplitudes. A dozen events in the last decade were identified to show high-quality single-event correlograms (Tkalčić and Phạm, 2020). Furthermore, to rule out the possible impact due to

608 numerical dispersion in the AxiSEM waveform simulation method, we compared the resultant
609 correlation wavefield with results obtained by the Yspec method (Al-Attar and Woodhouse, 2008) that
610 was employed to generate direct seismograms using the mode-summation method. We found almost
611 identical correlograms produced by the two independent methods, which ensures confidence in
612 utilizing the amplitudes of correlation features to infer Earth's interior properties.

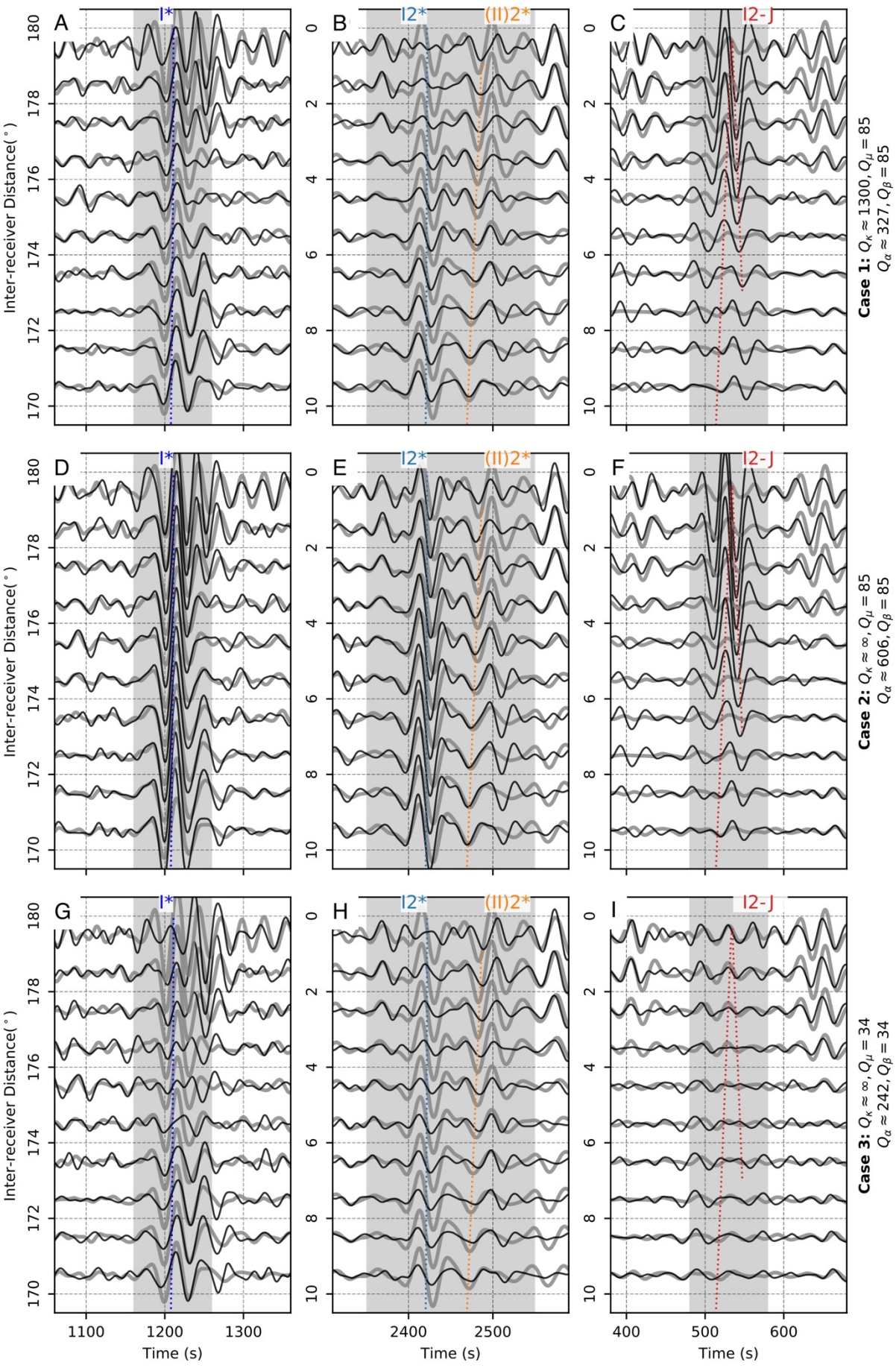
A
B
C
D
E
F
G
H
I
I*
I2*
(II)2*
I2-J
Inter-receiver Distance(°)
Time (s)
Case 1: $Q_\kappa \approx 1300, Q_\mu = 85$
$Q_\alpha \approx 327, Q_\beta = 85$
Case 2: $Q_\kappa \approx \infty, Q_\mu = 85$
$Q_\alpha \approx 606, Q_\beta = 85$
Case 3: $Q_\kappa \approx \infty, Q_\mu = 34$
$Q_\alpha \approx 242, Q_\beta = 34$

613

Figure 11

Comparison of waveforms for three attenuation models for the IC marked by diamonds in Figure 6. In each panel, the synthetic correlations are shown in black, while the observed correlations are gray. Left panels (A, D, G) focus on the I* correlation feature at near-antipodal inter-receiver distances, middle panels (B, E, H) focus on the I2* and (II)2* features at small inter-receiver distances, and right panels (C, F, I) focus on the I2-J feature. Three different IC attenuation models indicated on the right are used to produce synthetic waveforms. See Figure 6 for the illustration of compressional-wave quality factor (Q_α) as a function of bulk (Q_κ) and shear quality factors (Q_μ) for these 3 cases.

After careful consideration of the factors that can influence the correlation features' amplitudes, we attempt to use their amplitudes to constrain the IC's intrinsic attenuation. Firstly, the amplitudes of synthetic features calculated using ak135f (Montagner & Kennett, 1996) as an input model (Figure 10D, E) are benchmarked with their observed counterparts. We observe a reasonably good match for most features in the correlograms (proving the accuracy of the spherically symmetric models of the Earth at these frequencies) except for the four above-mentioned IC-sensitive features. Interestingly, in those figures, the binned correlation waveforms are compared in absolute amplitudes without any amplitude scaling. This is a good indication that the mantle and OC structure profiles are well constrained (Tkalčić and Phạm, 2018). However, the unmatched amplitudes of IC-related correlation features suggest that the IC properties require adjustments.

A closer look reveals that the synthetics computed in numerical simulations underestimate the amplitudes of the observed *I**, *I2** and *(II)2** (Figures 11A, B), suggesting that ak135f has too high IC P-wave attenuation, Q_P^{-1}, i.e., too low P-wave quality factor, Q_P (the ak135f's $Q_\alpha \approx 324$ given that $Q_\kappa \approx 600$ and $Q_\mu = 85$; marked as Case 1 in Figures 6 and 11). Note that Q_κ in the ak135f model is mistakenly copied from PREM's Q_P profile in the IC, which were inferred using Equation (4) assuming PREM wave speeds, as Montagner & Kennett (1996) were not attempting to constrain the cores' properties (Kennett, personal communication). By increasing Q_α in the IC to 600, which is done

via Equation (4) by setting $Q_\kappa > 10{,}000$ and keeping Q_μ unchanged (marked as Case 2 in Figures 6 and 11), we can improve the fit for these features (Figure 11D, E). Indeed, Case 2 is equivalent to having the IC attenuation properties original incorporated in PREM. However, for $Q_\mu \geq 85$ (Figure 11F), the amplitude of shear-sensitive feature I2-J is significantly overpredicted. If Q_μ is lowered relative to PREM, a reasonable amplitude fit for I2-J can be obtained (Figure 11G, H), albeit at the expense of underpredicting the amplitudes of the other three features (Figure 11I). In Case 3, $Q_\mu = 40$, which is approximately half of the PREM value.

Although we could not achieve satisfactory waveform fits for all four considered features simultaneously in this extended experiment, we are optimistic that the correlation wavefield method has great potential in the future research of Earth's IC (Tkalčić et al., 2020). As preliminarily demonstrated in Tkalčić and Phạm (2018) and further in Figure 11, the correlation feature *I2–J* and its remarkable sensitivity to IC's shear properties can be robustly synthesized and observed. This is in stark contrast to previous attempts to search for the J-wave footprint in the direct seismic wavefield (Figure 4), where the amplitudes of PKJKP waves lie under the observational threshold defined by the noise (Shearer et al. 2011). Namely, in the correlation wavefield, I2-J amplitudes are just an order of magnitude smaller than the mantle-sensitive features.

As we cannot model all IC-sensitive correlation features by forward-modeling IC compressional and shear properties simultaneously, this likely means that we have to rule out the simplified models for IC's shear properties. As presented above, a strongly attenuative, homogeneous, and isotropic inner core in shear cannot provide good simultaneous fits for the examined four features. The existence of heterogeneities in anisotropic velocity structure (e.g., Creager 1999; Frost et al. 2021; Tkalčić 2010), attenuation (e.g., Li and Cormier 2002; Attanayake et al. 2014, Iritani et al. 2014, Pejić et al., 2019, 2017), and compressional- and shear-wave anisotropy (Section 4) could reduce the amplitudes of I2-J

correlation features significantly. Therefore, with this in mind, the current full-waveform attempts to simulate the IC's shear structure must be intensified using both direct seismic and correlation wavefields.

5.2. Detecting J waves using modern seismic arrays

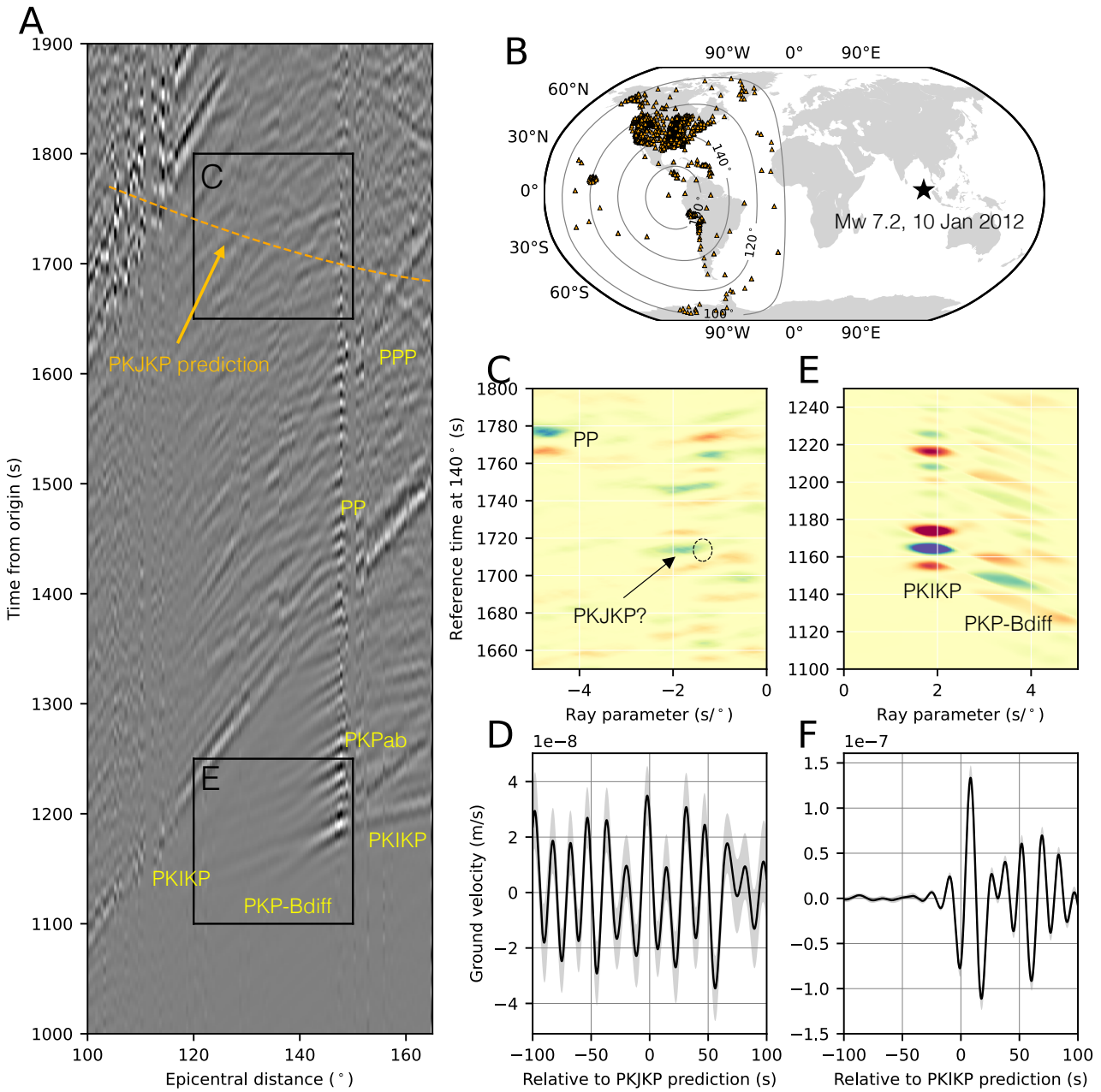

Figure 12

An attempt to observe PKJKP waves in a global seismic travel-time stack using large seismic arrays. A) A linear stack of vertical waveforms in 1-degree epicentral distance bins from the M_w=7.2 West of

675 Sumatra earthquake (10 Jan 2012). Yellow labels denote prominent seismic phases in this window.
676 Dashed orange line and label indicate the travel time curve of PKJKP waves predicted by the Earth
677 reference model ek137 (Kennett, 2020), which incorporates the updated IC's Vs profile proposed by
678 Tkalčić and Phạm (2018). The black rectangle boxes show the time and epicentral distance range of
679 waveforms used to compute the slant stack in panels C and E. The visible jump near the epicentral
680 distance of 150° is due to a sharp reduction in receiver numbers at the southern end of the US Array.
681 B) Map of stations and the earthquake used to construct the global stack in panel A. A black star
682 denotes the earthquake, while orange triangles mark stations. C) Second-order phase-weighted slant
683 stack is constructed from seismograms in epicentral distance range 120–150° surrounding the
684 predicted travel time curve of PKJKP (see the black box in panel A). Times are relative to an epicentral
685 distance of 140°. The dashed oval marks the PKJKP prediction by the reference model ek137. D) The
686 black line shows the linear waveform-stack in epicentral distance range 120–150° aligned relative to
687 PKJKP prediction. Light grey strip shows the uncertainty – two standard deviations – of the stacked
688 waveform estimated using the bootstrap sampling method (Efron and Tibshirani, 1991). E) and F) are
689 similar to C) and D) but for the window surrounding predicted PKIKP.
690

691 The global seismic network has expanded significantly in the last decades, including the initiation of
692 large dense seismic networks at regional and continental scales such as the Hi-net array covering Japan,
693 USArray covering the mainland US and Alaska, the ChinArray covering China, and multi-national
694 deployment of seismometers across Europe. Nowadays, an earthquake can be simultaneously observed
695 by thousands of seismic stations distributed globally (see Tkalčić and Phạm (2020) for an example of
696 a recent advance in the global correlation-wavefield theory and methodology using a single event). A
697 full-range seismic wavefield can be constructed by many seismic records from a single event instead
698 of stacking over multiple events as previously demonstrated by Shearer et al. (2011). Here, we are
699 inspired by Shearer et al. (2011) to scrutinize the possibility of detecting a footprint of J waves in the
700 direct seismic wavefield by taking advantage of an unprecedented number of receivers in the global
701 seismic networks.
702

703 We exploit more than 1500 broadband seismograms of the M_w=7.2 West of Sumatra earthquake of 10
704 January 2012 to produce a global waveform stack (Figure 12A). The selected earthquake location is
705 in the southern hemisphere to maximize the benefits of dense seismic arrays in the northern hemisphere
706 at the epicentral distance range suitable for J-wave observation (Figure 12B). The majority of the
707 seismograms were recorded by the USArray, which provides good coverage in the epicentral distance
708 range 120–150°, in which we expect the maximum amplitude for PKJKP waves (Doornbos, 1974). To
709 ensure the highest quality results, we retained only continuous 30-minute records since the event's
710 origin time. The data were then corrected for instrumental responses to obtain ground-velocity
711 seismograms and bandpass-filtered in the range 15–50 s. In Figure 12A, the processed seismograms
712 are grouped in 1-degree bins, and we use a median filter to remove unwanted seismograms with
713 possible glitches or other instrumental issues. Specifically, for each bin, the median of the maximum
714 absolute values of all seismograms is determined, and a seismogram in the bin is rejected if its
715 maximum absolute value is five times larger than the pre-determined median.
716
717 Figure 12A shows a waveform stack produced from a single earthquake with a prominent presence of
718 seismic phases at near-antipodal distances, such as PP, PPP, PKIKP, and PKP. We can observe a
719 suspected candidate for PKJKP signals around the theoretical prediction in the slant stack (Figure 12C),
720 although not so confidently in the waveform stack (Figure 12D). The theoretical prediction is based
721 on the reference model ek137 (Kennett, 2020), which employed the 2.5% reduction in the IC's shear-
722 wave speed relative to PREM proposed by Tkalčić and Phạm (2018). The PKIKP waves are shown
723 for comparison with PKJKP waves in Figures 12E and 12F. At present, we cannot provide further
724 evidence for the reliability of the observation of this PKJKP signal. Instead, we would like to encourage
725 other quests for PKJKP signals thanks to the availability of dense seismic networks.
726
727
728

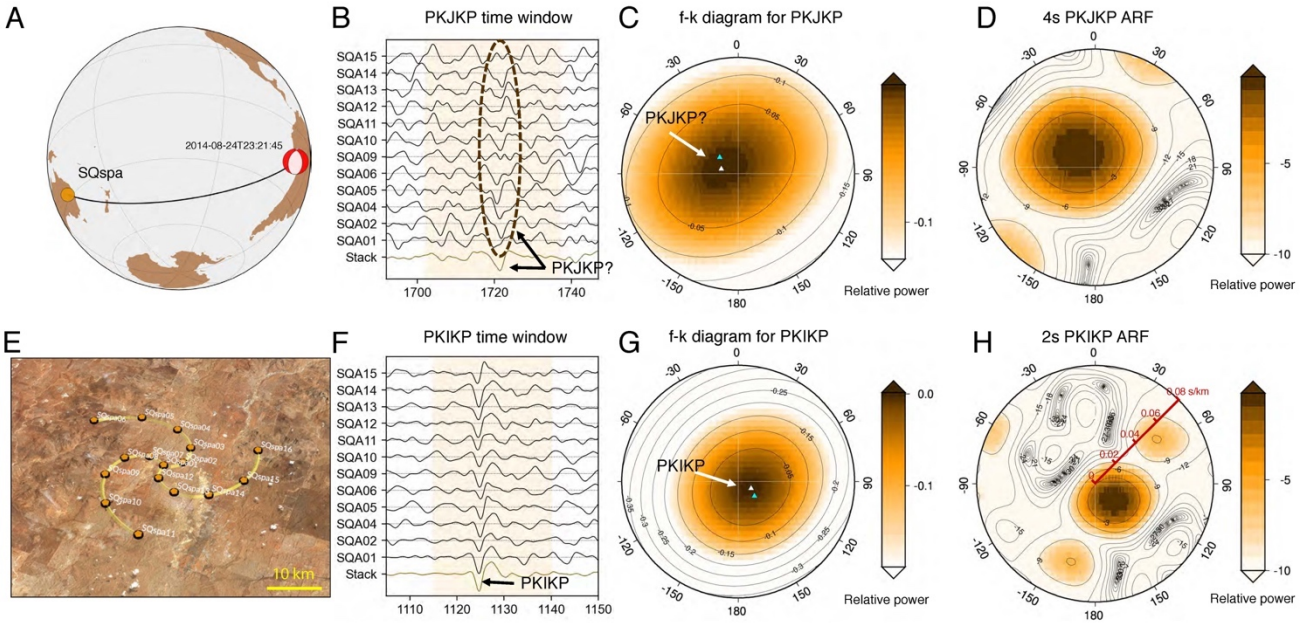

Figure 13

An attempt to observe PKJKP waves using a specially designed short-aperture, spiral-arm array. (A) Geographical locations of SQspa array and the M_w=6.8, 2014-08-24 central Peru event. (B) Vertical component seismograms in the time window around theoretical PKJKP arrival for the SQspa stations. The orange waveform at the bottom is the linear stack of all seismograms. The shaded area indicates the time window used for f-k analysis. The dashed ellipse indicates weak but coherent phases around the theoretical PKJKP arrival time. The phase is much clearer in the waveform stack. (C) The f-k diagram using the waveforms in (B). The light blue and white triangles indicate the predicted and the observed PKJKP arrivals, respectively. (D) The theoretical array response function for SQspa for a monochromatic 4 s PKJKP wave given the theoretical back azimuth and slowness for the 2014-08-24 event. (E) The local-scale map of the SQspa array. (F) Vertical component seismograms in the time window around theoretical PKIKP arrival time. The shadowed area indicates the time window used for f-k analysis. (G) The f-k diagram using the waveforms in (F). The light blue and white triangles indicate the predicted and the observed PKIKP arrivals, respectively. (H) The theoretical array response function for SQspa for a monochromatic 2 s PKIKP wave given the theoretical back azimuth and slowness for the 2014-08-24 event.

Finally, we present another likely PKJKP observation, this time using a short-aperture spiral-arm array in southern Queensland (SQspa; operated by RSES, ANU), designed to be compared with and to complement linear short-aperture arrays such as WRA in Northern Territory, a primary seismic station of the International Monitoring System. Spiral-arm arrays have a valuable property to suppress the

751 array response functions' side-lobes due to the versatility of inter-receiver vectors (Kennett et al. 2015;
752 Tkalčić 2017). SQspa has been utilized simultaneously with other arrays to enhance both signal quality
753 and resolution (Stipčević et al. 2017). Five such spiral arrays have already been deployed in Australia
754 (four by RSES, ANU, and one by Geoscience Australia), with a plan for another deployment in
755 Antarctica. Therefore, we can take advantage of a unique location in the southern hemisphere to
756 analyze the northern events in the epicentral distance range suitable for observing PKJKP waves.
757
758 In searching for PKJKP arrivals, we select global $M_w \geq 6.5$ events in the time interval 2014-2015 when
759 SQspa was in operation, from the epicentral distance range 120°–160°. We choose vertical component
760 seismograms and filter them using the 2-20 bandpass filter following Wookey and Helffrich (2008).
761 We first pre-process seismograms centered in a time window around the theoretical PKJKP arrival
762 time based on Tkalčić and Phạm (2018). After cutting the waveforms (see shaded areas in Figures 13B,
763 F), we compute the slowness diagrams using a frequency-domain f-k method (for a review of array
764 seismology, see Rost and Thomas 2002; also see Figures 2.8-2.12 in Tkalčić (2017), which illustrate
765 various arrays' response functions). In the back azimuth-slowness contour diagrams, seismic arrivals
766 manifest as energy peaks at the position quantified by slowness and back-azimuth measurements.
767 Hence, we can search for possible PKJKP arrivals based on the direction of the incoming seismic
768 energy.
769
770 Figure 13 shows an example of a possible PKJKP observation for August 24, 2014, M_w=6.8 event in
771 central Peru. A weak but coherent phase close to the theoretical PKJKP arrival time appears in the
772 waveforms on most of the stations, and it is much clearer and prominent in the linear stack (the bottom
773 waveform in Figure 13B). An energy peak close to theoretical PKJKP arrivals can also be seen in the
774 f-k diagram (Figure 13C). The slowness and back azimuth for the energy peak is close to theoretical
775 predictions. We compare the observational with the theoretical array response function for a

776 monochromatic 4 s plane wave for the 2014-08-24 event (Figure 13D). Notably, the obtained f-k
777 diagram is similar to the theoretical array response function for PKJKP. The observed energy peak
778 corresponding to PKJKP waves appears in approximately the same location of the f-k diagram as the
779 theoretical prediction. Furthermore, to check the reliability of our analysis, we conduct the same
780 analysis for PKIKP waves, a prominent seismic phase in raw seismograms (Figure 13F-H). The
781 comparison shows that our analysis can effectively record deep-earth seismic arrivals. However,
782 currently, we cannot provide more evidence for the captured PKJKP arrivals. Careful examination of
783 other seismograms in different locations is necessary to confirm this observation.
784
785 As the last section demonstrates, with the expansion of seismic networks, innovative methods, and
786 computing power, we enter a new era to discover and characterize IC's shear properties.
787
788
789 ## 6. SUMMARY
790 The current understanding of the IC shear properties from seismological observations can be
791 summarized as follows:
792
793 1. The IC is solid, which has been demonstrated through the seismological observations of Earth's
794 normal modes (T>100 s) and the existence of IC shear waves in both the seismic (down to T=2
795 s) and correlation wavefield (T=15-50 s).
796 2. The most recent observation points to shear-wave speeds and shear moduli of 3.42±0.02 km/s
797 and 149.0±1.6 GPa near the ICB and 3.58±0.02 km/s and 167.4±1.6 GPa in the Earth's center,
798 but further refinements are expected soon due to theoretical and methodological advances in
799 earthquake coda-correlation methods. In particular, one of the future goals is to constrain radial
800 dependence of IC shear-wave speed, e.g., in the uppermost IC where there is more sensitivity
801 of seismic probes and near the transition to the innermost IC.

3. Estimates of IC attenuation in shear have proven particularly challenging. The range of values for Q_μ from about 80 to 1000 has been proposed, and there is currently no consensus among seismological studies based on different frequency-band and depth sensitivities or between the seismological and mineral physics studies. In general, normal-mode observations require lower Q_μ than the body-wave observations and mineral-physics studies, and with the current sparsity of seismological observation and significant uncertainties in the IC mineral state, the reconciliation of these measurements is difficult. Coda-correlation has shown the potential to improve IC shear-attenuation estimates, and the ongoing research should refine estimates on its radial dependence.
4. There are only a couple of seismological observations of shear-wave anisotropy, one from the shear waves in the direct seismic wavefield and another from a coda-correlation study based on similarity of IC-sensitive seismic phases. Both agree on the inferred value of anisotropy strength of ~1%, but they cannot distinguish between the models for the stable phase of iron.
5. Further advances in this field will come from more high-quality data due to the expansion of seismic arrays and the proliferation of seismometers in remote areas of the planet and the ocean floor. This will improve our knowledge of the Earth's outer shells and enable further IC-sensitive seismological observations in all frequency bands by multiple methods, some of which were discussed in this review paper. Finally, it is expected that mineral physics will advance in the coming decade to the point that high-pressure/high-temperature experiments will become more common for the IC conditions. This will help remove large uncertainties on multiple physical parameters, including shear properties and the stable mineralogical phase of iron.

DISCLOSURE STATEMENT

The authors are not aware of any affiliations, memberships, funding, or financial holdings that might be perceived as affecting the objectivity of this review.

828
829

ACKNOWLEDGMENTS

Most of the global waveform data shown or mentioned in this review are available through the Incorporated Research Institutions for Seismology (IRIS; www.iris.edu) through the Data Management Center. The facilities of IRIS Data Services, and specifically the IRIS Data Management Center, were used for access to waveforms, related metadata, and/or derived products used in this study. IRIS Data Services are funded through the Seismological Facilities for the Advancement of Geoscience (SAGE) Award of the National Science Foundation under Cooperative Support Agreement EAR-1851048. H.T. is also grateful to the Australian Research Council for supporting seismological research on deep Earth under previous and current grants and to AuScope, Inc. for continuing support. The SQspa array was funded under the ARC Discovery Grant DP130101473: "Multi-array, multi-frequency probing of the Earth's heterogeneity". The authors are grateful to AusPass, an initiative supported with funding from AuScope and the Australian National University to provide access to broadband passive seismic data collected in Australia since 1997. To facilitate knowledge discovery and innovation, AusPass adopts and supports FAIR data principles. Special thanks to V.F. Cormier for insightful discussions on the IC topic, to M. Mattesini for his instructions on reproducing theoretical predictions for IC anisotropic crystals, and to J. Wookey and G. Helffrich for allowing us to reproduce their published figures. Last but not least, H.T. would like to acknowledge graduate students, postdoctoral fellows, and faculty of the Geophysics area at RSES, and the ANU Media team, for shown interest in research on the IC subject.

LITERATURE CITED

Al-Attar D, Woodhouse JH. 2008. Calculation of seismic displacement fields in self-gravitating earth models—applications of minors vectors and symplectic structure. *Geophysical Journal International*. 175(3):1176–1208

Alterman Z, Jarosch H, Pekeris CL, Jeffreys H. 1959. Oscillations of the earth. *Proceedings of the Royal Society of London. Series A. Mathematical and Physical Sciences*. 252(1268):80–95

Anderson DL, Hart RS. 1978. Attenuation models of the earth. *Physics of the Earth and Planetary Interiors*. 16(4):289–306

Andrews J, Deuss A, Woodhouse J. 2006. Coupled normal-mode sensitivity to inner-core shear velocity and attenuation. *Geophysical Journal International*. 167(1):204–12

Antonangeli D, Merkel S, Farber DL. 2006. Elastic anisotropy in hcp metals at high pressure and the sound wave anisotropy of the Earth's inner core. *Geophysical Research Letters*. 33(24):

Antonangeli D, Occelli F, Requardt H, Badro J, Fiquet G, Krisch M. 2004. Elastic anisotropy in textured hcp-iron to 112 GPa from sound wave propagation measurements. *Earth and Planetary Science Letters*. 225(1):243–51

Attanayake J, Cormier VF, de Silva SM. 2014. Uppermost inner core seismic structure – new insights from body waveform inversion. *Earth and Planetary Science Letters*. 385:49–58

Aubert J, Amit H, Hulot G, Olson P. 2008. Thermochemical flows couple the Earth's inner core growth to mantle heterogeneity. *Nature*. 454(7205):758–61

Backus GE. 1965. Possible forms of seismic anisotropy of the uppermost mantle under oceans. *Journal of Geophysical Research (1896-1977)*. 70(14):3429–39

Belonoshko AB, Fu J, Bryk T, Simak SI, Mattesini M. 2019. Low viscosity of the Earth's inner core. *Nature Communications*. 10(1):2483

Belonoshko AB, Skorodumova NV, Davis S, Osiptsov AN, Rosengren A, Johansson B. 2007. Origin of the Low Rigidity of the Earth's Inner Core. *Science*. 316(5831):1603–5

876 Belonoshko AB, Skorodumova NV, Rosengren A, Johansson B. 2008. Elastic Anisotropy of Earth's
877 Inner Core. *Science*. 319(5864):797–800
878 Benioff H, Press F, Smith S. 1961. Excitation of the free oscillations of the Earth by earthquakes.
879 *Journal of Geophysical Research (1896-1977)*. 66(2):605–19
880 Bergman MI. 1997. Measurements of electric anisotropy due to solidification texturing and the
881 implications for the Earth's inner core. *Nature*. 389(6646):60–63
882 Biggin AJ, Piispa EJ, Pesonen LJ, Holme R, Paterson GA, et al. 2015. Palaeomagnetic field intensity
883 variations suggest Mesoproterozoic inner-core nucleation. *Nature*. 526(7572):245–48
884 Birch AF. 1940. The alpha-gamma transformation of iron at high pressures, and the problem of the
885 earth's magnetism. *American Journal of Science*. 238(3):192–211
886 Birch F. 1952. Elasticity and constitution of the Earth's interior. *Journal of Geophysical Research*
887 *(1896-1977)*. 57(2):227–86
888 Braginsky SI. 1963. Structure of the F layer and reasons for convection in the Earth's core. *Soviet*
889 *Physics Doklady* 149:8–10
890 Buffett BA, Huppert HE, Lister JR, Woods AW. 1996. On the thermal evolution of the Earth's core.
891 *Journal of Geophysical Research: Solid Earth*. 101(B4):7989–8006
892 Buffett BA, Wenk H-R. 2001. Texturing of the Earth's inner core by Maxwell stresses. *Nature*.
893 413(6851):60–63
894 Bullen KE. 1946. A Hypothesis on Compressibility at Pressures of the Order of a Million
895 Atmospheres. *Nature*. 157(3987):405–405
896 Bullen KE. 1950. Theoretical Travel-Times of S Waves in the Earth's Inner Core. *Geophysical*
897 *Journal International*. 6(s2):125–28
898 Bullen KÈ. 1951. Theoretical Amplitudes of the Seismic Phase Pkjkp. *Geophysical Journal*
899 *International*. 6(s3):163–67

900 Calvet M, Margerin L. 2008. Constraints on grain size and stable iron phases in the uppermost inner
901 core from multiple scattering modeling of seismic velocity and attenuation. *Earth and*
902 *Planetary Science Letters*. 267(1):200–212
903 Cao A. 2005. An Observation of PKJKP: Inferences on Inner Core Shear Properties. *Science*.
904 308(5727):1453–55
905 Cao A, Romanowicz B. 2009. Constraints on shear wave attenuation in the Earth's inner core from
906 an observation of PKJKP. *Geophysical Research Letters*. 36(9):
907 Cormier VF. 2015. Detection of inner core solidification from observations of antipodal PKIIKP.
908 *Geophysical Research Letters*. 42(18):7459–66
909 Cormier VF. 2020. Seismic Viscoelastic Attenuation. In *Encyclopaedia of Solid Earth Geophysics*,
910 ed. HK Gupta, pp. 1–14. Cham: Springer International Publishing
911 Crampin S. 1977. A review of the effects of anisotropic layering on the propagation of seismic
912 waves. *Geophysical Journal International*. 49(1):9–27
913 Creager KC. 1999. Large-scale variations in inner core anisotropy. *Journal of Geophysical*
914 *Research: Solid Earth*. 104(B10):23127–39
915 Dahlen FA, Tromp J. 1998. *Theoretical Global Seismology*. Princeton, N.J: Princeton University
916 Press
917 de Wit RWL, Käufl PJ, Valentine AP, Trampert J. 2014. Bayesian inversion of free oscillations for
918 Earth's radial (an)elastic structure. *Physics of the Earth and Planetary Interiors*. 237:1–17
919 Deguen R. 2012. Structure and dynamics of Earth's inner core. *Earth and Planetary Science Letters*.
920 333–334:211–25
921 Derr JS. 1969. Internal structure of the Earth inferred from free oscillations. *Journal of Geophysical*
922 *Research (1896-1977)*. 74(22):5202–20
923 Deuss A. 2014. Heterogeneity and Anisotropy of Earth's Inner Core. *Annual Review of Earth and*
924 *Planetary Sciences*. 42(1):103–26

925 Deuss A, Woodhouse JH, Paulssen H, Trampert J. 2000. The observation of inner core shear waves.
926 *Geophysical Journal International*. 142(1):67–73
927 Doornbos DJ. 1974. The Anelasticity of the Inner Core. *Geophysical Journal International.*
928 38(2):397–415
929 Dziewonski AM. 1971. Overtones of Free Oscillations and the Structure of the Earth's Interior.
930 *Science*. 172(3990):1336–38
931 Dziewonski AM, Anderson DL. 1981. Preliminary reference Earth model. *Physics of the Earth and*
932 *Planetary Interiors*. 25(4):297–356
933 Dziewonski AM, Gilbert F. 1971. Solidity of the Inner Core of the Earth inferred from Normal Mode
934 Observations. *Nature*. 234(5330):465–66
935 Fischer RA, Campbell AJ. 2015. The axial ratio of hcp Fe and Fe–Ni–Si alloys to the conditions of
936 Earth's inner core. *American Mineralogist*. 100(11–12):2718–24
937 Frost DA, Lasbleis M, Chandler B, Romanowicz B. 2021. Dynamic history of the inner core
938 constrained by seismic anisotropy. *Nature Geoscience.* 1–5
939 Fukao Y, Suda N. 1989. Core modes of the Earth's free oscillations and structure of the inner core.
940 *Geophysical Research Letters*. 16(5):401–4
941 Gubbins D, Sreenivasan B, Mound J, Rost S. 2011. Melting of the Earth's inner core. *Nature*.
942 473(7347):361–63
943 Hirose K, Labrosse S, Hernlund J. 2013. Composition and State of the Core. *Annual Reviews of*
944 *Earth and Planetary Sciences.* 41(1):657–91
945 Hollerbach R, Jones CA. 1993. Influence of the Earth's inner core on geomagnetic fluctuations and
946 reversals. *Nature*. 365(6446):541–43
947 Iritani R, Takeuchi N, Kawakatsu H. 2014. Intricate heterogeneous structures of the top 300km of
948 the Earth's inner core inferred from global array data: I. Regional 1D attenuation and velocity
949 profiles. *Physics of the Earth and Planetary Interiors*. 230:15–27

Jeanloz R, Wenk H-R. 1988. Convection and anisotropy of the inner core. *Geophysical Research Letters*. 15(1):72–75

Julian BR, Davies D, Sheppard RM. 1972. PKJKP. *Nature*. 235(5337):317–18

Karato S. 1993. Inner Core Anisotropy Due to the Magnetic Field—induced Preferred Orientation of Iron. *Science*. 262(5140):1708–11

Karato S. 1999. Seismic anisotropy of the Earth's inner core resulting from flow induced by Maxwell stresses. *Nature*. 402(6764):871–73

Karato S. 2008. *Deformation of Earth Materials: An Introduction to the Rheology of Solid Earth*. Cambridge: Cambridge University Press

Kennett BLN. 2020. Radial earth models revisited. *Geophysical Journal International*. 222(3):2189–2204

Kennett BLN, Engdahl ER, Buland R. 1995. Constraints on seismic velocities in the Earth from traveltimes. *Geophysical Journal International*. 122(1):108–24

Kennett BLN, Fichtner A. 2021. *Exploiting Seismic Waveforms Correlations, Heterogeneity and Inversion*

Kennett BLN, Stipčević J, Gorbatov A. 2015. Spiral-Arm Seismic Arrays. *Bulletin of the Seismological Society of America*. 105(4):2109–16

Krasnoshchekov DN, Ovtchinnikov VM, Usoltseva OA. 2019. Shear Wave Velocity in the Top of the Earth's Inner Core. *Doklady Earth Sciences.* 488(2):1186–89

Lehmann I. 1936. P'. *Publications Du Bureau Central Seismologique International, Série A,Travaux Scientifique*. (14):87–115

Li X, Cormier VF. 2002. Frequency-dependent seismic attenuation in the inner core, 1. A viscoelastic interpretation. *Journal of Geophysical Research: Solid Earth*. 107(B12):ESE 13-1-ESE 13-20

974 Lin J-F, Mao Z, Yavaş H, Zhao J, Dubrovinsky L. 2010. Shear wave anisotropy of textured hcp-Fe
975 in the Earth's inner core. *Earth and Planetary Science Letters*. 298(3):361–66
976 Mao H, Shu J, Shen G, Hemley RJ, Li B, Singh AK. 1998. Elasticity and rheology of iron above 220
977 GPa and the nature of the Earth's inner core. *Nature*. 396(6713):741–43
978 Mao WL, Campbell AJ, Heinz DL, Shen G. 2006. Phase relations of Fe–Ni alloys at high pressure
979 and temperature. *Physics of the Earth and Planetary Interiors*. 155(1):146–51
980 Masters G, Gilbert F. 1981. Structure of the inner core inferred from observations of its spheroidal
981 shear modes. *Geophysical Research Letters*. 8(6):569–71
982 Masters TG, Shearer PM. 1990. Summary of seismological constraints on the structure of the Earth's
983 core. *Journal of Geophysical Research: Solid Earth*. 95(B13):21691–95
984 Mattesini M, Belonoshko AB, Buforn E, Ramírez M, Simak SI, et al. 2010. Hemispherical
985 anisotropic patterns of the Earth's inner core. *Proceedings of National Academy of Science*.
986 107(21):9507–12
987 Mattesini M, Belonoshko AB, Tkalčić H, Buforn E, Udias A, Ahuja R. 2014. Candy wrapper for the
988 Earth's inner core. *Scientific Reports*, 3:2096
989 Montagner J-P, Kennett BLN. 1996. How to reconcile body-wave and normal-mode reference earth
990 models. *Geophysical Journal International*. 125(1):229–48
991 Morelli A, Dziewonski AM, Woodhouse JH. 1986. Anisotropy of the inner core inferred from
992 PKIKP travel times. *Geophysical Research Letters*. 13(13):1545–48
993 Nissen-Meyer T, van Driel M, Stähler SC, Hosseini K, Hempel S, et al. 2014. AxiSEM: broadband
994 3-D seismic wavefields in axisymmetric media. *Solid Earth*. 5(1):425–45
995 Okal EA, Cansi Y. 1998. Detection of PKJKP at intermediate periods by progressive multi-channel
996 correlation. *Earth and Planetary Science Letters*. 164(1):23–30

997 Pejić T, Hawkins R, Sambridge M, Tkalčić H. 2019. Transdimensional Bayesian Attenuation
998 Tomography of the Upper Inner Core. *Journal of Geophysical Research: Solid Earth*.
999 124(2):1929–43
1000 Pejić T, Tkalčić H, Sambridge M, Cormier VF, Benavente R. 2017. Attenuation tomography of the
1001 upper inner core. *Journal of Geophysical Research: Solid Earth*. 122(4):3008–32
1002 Phạm T-S, Tkalčić H, Sambridge M, Kennett BLN. 2018. Earth's Correlation Wavefield: Late Coda
1003 Correlation. *Geophysical Research Letters*. 45(7):3035–42
1004 Poupinet G, Pillet R, Souriau A. 1983. Possible heterogeneity of the Earth's core deduced from
1005 PKIKP travel times. *Nature*. 305(5931):204–6
1006 Resovsky J, Trampert J, Van der Hilst RD. 2005. Error bars for the global seismic Q profile. *Earth*
1007 *and Planetary Science Letters*. 230(3):413–23
1008 Roberts AP. 2008. Geomagnetic excursions: Knowns and unknowns. *Geophysical Research Letters*.
1009 35(17):
1010 Romanowicz BA, Mitchell BJ. 2015. 1.25 - Deep Earth Structure: Q of the Earth from Crust to Core.
1011 In *Treatise on Geophysics (Second Edition)*, ed. G Schubert, pp. 789–827. Oxford: Elsevier
1012 Rost S, Thomas C. 2002. Array Seismology: Methods and Applications. *Reviews of Geophysics*.
1013 40(3):2-1-2–27
1014 Shearer PM. 2009. *Introduction to Seismology*. Cambridge: Cambridge University Press. 2nd ed.
1015 Shearer PM, Rychert CA, Liu Q. 2011. On the visibility of the inner-core shear wave phase PKJKP
1016 at long periods. *Geophysical Journal International*. 185(3):1379–83
1017 Singh SC, Taylor M a. J, Montagner JP. 2000. On the Presence of Liquid in Earth's Inner Core.
1018 *Science*. 287(5462):2471–74
1019 Song X. 1997. Anisotropy of the Earth's inner core. *Reviews of Geophysics*. 35(3):297–313
1020 Souriau A, Calvet M. 2015. 1.23 - Deep Earth Structure: The Earth's Cores. In *Treatise on*
1021 *Geophysics (Second Edition)*, ed. G Schubert, pp. 725–57. Oxford: Elsevier

1022 Steinle-Neumann G, Stixrude L, Cohen RE, Gülseren O. 2001. Elasticity of iron at the temperature
1023 of the Earth's inner core. *Nature*. 413(6851):57–60
1024 Stipčević J, Kennett BLN, Tkalčić H. 2017. Simultaneous use of multiple seismic arrays.
1025 *Geophysical Journal International*. 209(2):770–83
1026 Stixrude L, Cohen RE. 1995. High-Pressure Elasticity of Iron and Anisotropy of Earth's Inner Core.
1027 *Science*. 267(5206):1972–75
1028 Sumita I, Bergman M. 2015. 8.12 - Inner Core Dynamics. In *Treatise on Geophysics (Second*
1029 *Edition)*, ed. G Schubert, pp. 297–316. Oxford: Elsevier
1030 Talavera-Soza S, Deuss A. 2020. Constraining 1-D inner core attenuation through measurements of
1031 strongly coupled normal mode pairs. *Geophysical Journal International*. 223(1):612–21
1032 Tkalčić H. 2010. Large variations in travel times of mantle-sensitive seismic waves from the South
1033 Sandwich Islands: Is the Earth's inner core a conglomerate of anisotropic domains?
1034 *Geophysical Research Letters*. 37(14):
1035 Tkalčić H. 2015. Complex inner core of the Earth: The last frontier of global seismology. *Reviews of*
1036 *Geophysics*. 53(1):59–94
1037 Tkalčić H. 2017. *The Earth's Inner Core: Revealed by Observational Seismology*. Cambridge ; New
1038 York, NY: Cambridge University Press
1039 Tkalčić H, Phạm T-S. 2018. Shear properties of Earth's inner core constrained by a detection of J
1040 waves in global correlation wavefield. *Science*. 362(6412):329–32
1041 Tkalčić H, Phạm T-S. 2020. Excitation of the global correlation wavefield by large earthquakes.
1042 *Geophysical Journal International*. 223(3):1769–79
1043 Tkalčić H, Phạm T-S, Wang S. 2020. The Earth's coda correlation wavefield: Rise of the new
1044 paradigm and recent advances. *Earth-Science Reviews*. 208:103285
1045 Vallée M, Douet V. 2016. A new database of source time functions (STFs) extracted from the
1046 SCARDEC method. *Physics of the Earth and Planetary Interiors*. 257:149–57

1047 Vočadlo L. 2007. Ab initio calculations of the elasticity of iron and iron alloys at inner core
1048 conditions: Evidence for a partially molten inner core? *Earth and Planetary Science Letters*.
1049 254(1):227–32
1050 Vočadlo L, Alfè D, Gillan MJ, Wood IG, Brodholt JP, Price GD. 2003. Possible thermal and
1051 chemical stabilization of body-centred-cubic iron in the Earth's core. *Nature*. 424(6948):536–
1052 39
1053 Vočadlo L, Dobson DP, Wood IG. 2009. Ab initio calculations of the elasticity of hcp-Fe as a
1054 function of temperature at inner-core pressure. *Earth and Planetary Science Letters*.
1055 288(3):534–38
1056 Wang S, Tkalčić H. 2021. Shear-wave anisotropy in the Earth's inner core. *Geophysical Research*
1057 *Letters, revised.*
1058 Wang S, Tkalčić H. 2020. Seismic event coda-correlation's formation: implications for global
1059 seismology. *Geophysical Journal International*. 222(2):1283–94
1060 Waszek L, Deuss A. 2015. Observations of exotic inner core waves. *Geophysical Journal*
1061 *International*. 200(3):1636–50
1062 Wenk H-R, Matthies S, Hemley RJ, Mao H-K, Shu J. 2000. The plastic deformation of iron at
1063 pressures of the Earth's inner core. *Nature*. 405(6790):1044–47
1064 Wenk H-R, Baumgardner JR, Lebensohn RA, Tomé CN. 2000. A convection model to explain
1065 anisotropy of the inner core. *Journal of Geophysical Research: Solid Earth*. 105(B3):5663–77
1066 Widmer R, Masters G, Gilbert F. 1991. Spherically symmetric attenuation within the Earth from
1067 normal mode data. *Geophysical Journal International*. 104(3):541–53
1068 Woodhouse JH, Giardini D, Li X-D. 1986. Evidence for inner core anisotropy from free oscillations.
1069 *Geophysical Research Letters*. 13(13):1549–52
1070 Wookey J, Helffrich G. 2008. Inner-core shear-wave anisotropy and texture from an observation of
1071 PKJKP waves. *Nature*. 454(7206):873–76

1072 Yoshida S, Sumita I, Kumazawa M. 1996. Growth model of the inner core coupled with the outer
1073 core dynamics and the resulting elastic anisotropy. *Journal of Geophysical Research: Solid*
1074 *Earth*. 101(B12):28085–103
1075